Published in final edited form as:

Nat Med. 2015 November ; 21(11): 1262–1271. doi:10.1038/nm.3961.

Excess TGF-β mediates muscle weakness associated with bone metastases in mice

David L. Waning[#1], **Khalid S. Mohammad**[#1], **Steven Reiken**[2], **Wenjun Xie**[2], **Daniel C. Andersson**[2,8], **Sutha John**[1], **Antonella Chiechi**[1], **Laura E. Wright**[1], **Alisa Umanskaya**[2], **Maria Niewolna**[1], **Trupti Trivedi**[1], **Sahba Charkhzarrin**[1], **Pooja Khatiwada**[1], **Anetta Wronska**[2], **Ashley Haynes**[2], **Maria Serena Benassi**[3], **Frank A. Witzmann**[4], **Gehua Zhen**[5], **Xiao Wang**[5], **Xu Cao**[5], **G. David Roodman**[6,7], **Andrew R. Marks**[2], and **Theresa A. Guise**[1]

[1] Department of Medicine, Indiana University School of Medicine, Indianapolis, Indiana, USA.

[2] Department of Physiology and Cellular Biophysics, Helen and Clyde Wu Center for Molecular Cardiology, College of Physicians and Surgeons, Columbia University, New York, New York, USA.

[3] Laboratory of Experimental Oncology, Instituto Ortopedico Rizzoli, Bologna, Italy.

[4] Department of Cellular and Integrative Physiology, Indiana University School of Medicine, Indianapolis, Indiana, USA.

[5] Department of Orthopaedic Surgery, Johns Hopkins University School of Medicine, Baltimore, Maryland, USA

[6] Department of Medicine, Division of Hematology/Oncology, Indiana University School of Medicine, Indianapolis, Indiana, USA.

[7] Richard L. Roudebush VA Medical Center, Indianapolis, Indiana, USA.

[#] These authors contributed equally to this work.

Abstract

Cancer-associated muscle weakness is poorly understood and there is no effective treatment. Here, we find that seven different mouse models of human osteolytic bone metastases, representing breast, lung and prostate cancers, as well as multiple myeloma exhibited impaired muscle

Corresponding author: Theresa A. Guise, tguise@iu.edu.

[8]Present Address: Department of Medicine/Cardiology Unit and Department of Physiology and Pharmacology, Karolinska Institute, SE-17177 Stockholm, Sweden.

AUTHOR CONTRIBUTIONS

All contributing authors have agreed to submission of this manuscript for publication. T.A.G. and A.R.M. conceived of the study. D.L.W., K.S.M., A.R.M and T.A.G. designed experiments, performed experiments, analyzed data and interpreted results. S.R., W.X., D.C.A., S.J., M.N., A.C., L.E.W., A.U., T.T., S.C., F.A.W. and P.K. performed experiments. M.S.B. analyzed data. G.D.R. and F.A.W. designed experiments and interpreted results. G.Z., X.W., and X.C. provided CED mice and reviewed results and manuscript. D.L.W, K.S.M., A.R.M and T.A.G wrote the manuscript.

COMPETING FINANCIAL INTERESTS

A.R.M. is a member of the board and consults for ARMGO Pharma Inc. a startup company developing RyR targeted therapeutics; T.A.G. was a consultant/advisory board member for Novartis.

function, implicating a role for the tumor-bone microenvironment in cancer-associated muscle weakness. We found that TGF-β, released from the bone surface as a result of metastasis-induced bone destruction upregulated NADPH oxidase 4 (Nox4), resulting in elevated oxidization of skeletal muscle proteins, including the ryanodine receptor/calcium (Ca^{2+}) release channel (RyR1). The oxidized RyR1 channels leaked Ca^{2+}, resulting in lower intracellular signaling required for proper muscle contraction. We found that inhibiting RyR1 leak, TGF-β signaling, TGF-β release from bone or Nox4 all improved muscle function in mice with MDA-MB-231 bone metastases. Humans with breast cancer- or lung cancer-associated bone metastases also had oxidized skeletal muscle RyR1 that is not seen in normal muscle. Similarly, skeletal muscle weakness, higher levels of Nox4 protein and Nox4 binding to RyR1, and oxidation of RyR1 were present in a mouse model of Camurati-Engelmann disease, a non-malignant metabolic bone disorder associated with increased TGF-β activity. Thus, metastasis-induced TGF-β release from bone contributes to muscle weakness by decreasing Ca^{2+}-induced muscle force production.

Skeletal muscle weakness is a debilitating consequence of advanced malignancies, which are often associated with bone metastases. Research and therapy have focused on increasing muscle mass in humans with cancer-associated skeletal muscle weakness[1], but it is unclear whether a gain of mass alone will improve muscle function[2,3]. Moreover, little is known about whether tumors and their associated metastases cause muscle dysfunction resulting in weakness, or whether cancer-associated weakness is due solely to loss of muscle mass? Therefore, we investigated whether there is a cause of muscle weakness, independent of loss of muscle mass, in mouse models of human cancers with bone metastases.

Individuals with advanced cancer, including breast, prostate and lung, often have bone metastases and muscle weakness. In the tumor-bone microenvironment cancer cells, including those in patients with multiple myeloma, secrete factors that stimulate osteoclastic bone resorption, resulting in skeletal complications of bone pain, fractures, hypercalcemia, nerve compression syndromes and muscle weakness[4]. Osteoclastic bone resorption releases growth factors stored in the bone matrix, principally transforming growth factor-β (TGF-β), that further promote cancer cell invasion, growth and osteolytic factor production to fuel a feed-forward cycle that induces more bone destruction and tumor growth[4-7]. Bone resorption and formation is dynamically coupled by TGF-β[8]. Pathologically increased TGF-β release from bone, due to tumor-induced osteolysis, could be contributing to muscle weakness. In this study we found that mouse models of human breast, lung and prostate cancers, as well as multiple myeloma, in which mice develop osteolytic bone metastases, exhibit profound skeletal muscle weakness. We report that pathologically increased TGF-β release from bone causes muscle weakness by inducing intracellular calcium (Ca^{2+}) leak via NADPH oxidase 4 (Nox4)-mediated oxidation of the ryanodine receptor/Ca^{2+} release channel (RyR1) on the sarcoplasmic reticulum (SR). In normal muscle activation of RyR1 results in the release of SR Ca^{2+} that is the required signal triggering skeletal muscle contraction[9]. Pathological oxidation of RyR1 results in leaky channels that contribute to muscle weakness[10]. In the present study we show that targeting intracellular Ca^{2+} leak, increased bone resorption and increased TGF-β activity as well as Nox4 can all prevent muscle weakness in mice with MDA-MB-231 breast cancer bone metastases. Furthermore, higher Nox4 protein levels, increased Nox4 binding to RyR1, oxidation of RyR1, and

muscle weakness, all were obserevd in a mouse model of Camurati-Engelmann disease (CED), a non-malignant metabolic bone disorder associated with increased TGF-β activity and bone destruction. These findings raise the possibility that increased bone destruction and associated elevations in TGF-β activity can induce skeletal muscle weakness by oxidation of RyR1 and resultant Ca^{2+} leak. Thus, targeting any portion of this pathway might be beneficial to ameliorate muscle weakness in cancer patients with bone metastases.

RESULTS

Weakness and RyR1 oxidation in mice with bone metastases

To explore the basis for cancer-associated muscle weakness we used a mouse model of human breast cancer (MDA-MB-231) that causes osteolytic bone metastases and muscle weakness (**Supplementary Fig. 1a**)[11]. We inoculated 5-week-old female nude mice with 100,000 MDA-MB-231 cells via the left cardiac ventricle and found that mice had bone metastases, reduced body weight, fat and lean content (**Supplementary Fig. 1b**), as well as lower skeletal muscle mass 4 weeks post tumor inoculation compared to non-tumor control mice (**Supplementary Fig. 1c–d**). These mice all developed bone metastases and muscle weakness (reduction in forelimb grip strength) (**Fig. 1a**) and lower *ex vivo* muscle specific force, which represents muscle force corrected for changes in muscle size, of the extensor digitorum longus (EDL) compared to non-tumor control mice (**Fig. 1b**). Peak tetanic Ca^{2+} determines muscle force and was also lower compared to non-tumor bearing control mice (**Fig. 1c**) Thus, in addition to loss of muscle mass, mice with breast cancer bone metastases had loss of muscle function.

Advanced breast cancer is characterized by increased oxidative stress[12]. We used an unbiased mass spectrometry based screen to assess post-translational modifications of proteins in whole skeletal muscle lysates from mice with bone metastases compared with non-tumor bearing controls (**Supplementary Tables 1** and **2**). Measurement of the total carbonyl concentration in skeletal muscle lysates also showed that skeletal muscle from mice and from humans with tumors metastatic to bone exhibited higher skeletal muscle protein oxidation compared to muscle from mice and humans without bone metastases (**Supplementary Table 3**). Among skeletal muscle proteins that were nitrosylated or oxidized in mice with bone metastases were proteins involved in muscle contraction (**Supplementary Tables 1** and **2**). These included sarcomeric proteins (for example, tropomyosin and myosin), as well as the RyR1 Ca^{2+} release channel, which was identified as being both nitrosylated and oxidized (**Supplementary Tables 1** and **2**). Given that tetanic Ca^{2+} was lower in mice with MDA-MB-231 bone metastases than non-tumor control mice,, we focused on RyR1 as this channel is the source of Ca^{2+} release from the SR in skeletal muscle. Oxidation of RyR1 channels in skeletal muscle results in a pathological SR Ca^{2+} leak associated with muscle weakness[10,13]. Indeed, skeletal muscle RyR1 channels from mice with bone metastases were oxidized, nitrosylated, and depleted of the stabilizing subunit calstabin1 (also known as FKBP12) compared to non-tumor control mice (the biochemical signature of leaky channels) (**Fig. 1d**). These oxidation-induced changes in RyR1 were progressive over four weeks post tumor inoculation during the development of bone metastases (**Supplementary Fig. 1e**), and were associated with lower muscle specific

force in mice with breast cancer bone metastases compared to non-tumor control mice (**Supplementary Fig. 1f**). Mice with MDA-MB-231 breast cancer bone metastases had large osteolytic lesions by X-ray and the degree of muscle weakness correlated with the amount of bone destruction four weeks post tumor inoculation (**Supplementary Fig. 1g–h**). To determine whether the RyR1 modifications observed in the mouse models were relevant to human cancer we examined skeletal muscle RyR1 from humans with breast cancer-associated bone metastases and lung cancer-associated bone metastases and found the same post-translational modifications (oxidation and nitrosylation of RyR1 and lower calstabin1 binding) compared to humans without bone metastases, hereafter referred to as the biochemical signature of leaky RyR1 channels (**Fig. 1e–f**).

Muscle weakness associated with bone metastases

Since muscle weakness strongly correlated with bone destruction (**Supplementary Fig. 1h**), we investigated whether the tumor-bone microenvironment plays a role in cancer-associated muscle weakness. We inoculated 1,000,000 MDA-MB-231 cells (10-fold more cells than used in the bone metastases model) into the mammary fat pad which causes primary breast cancer only[14] and no bone metastases. In contrast to mice with bone metastases, mice with primary MDA-MB-231 mammary tumors (mean tumor mass 400 ± 91 mg) had normal muscle function (**Fig. 1g**), muscle mass, body weight and body composition (**Supplementary Fig. 1i–j**). Importantly, in contrast to mice with bone metastases, mice with primary tumors did not exhibit the biochemical signature of leaky RyR1 channels (**Fig. 1h**). These data suggest that the tumor-bone microenvironment plays a critical role in the development of cancer-associated muscle weakness.

In the present study we used mice with bone metastases due to seven different forms of human cancers including: MDA-MB-231 breast cancer, MCF-7 breast cancer, ZR75-1 breast cancer, A549 lung cancer, RWGT2 lung cancer[15], PC-3 prostate cancer and JJN-3 multiple myeloma. We sought to determine whether oxidative modifications of RyR1 and muscle weakness are common to diverse malignancies associated with bone destruction. These cancer models all have bone metastases with components of ostelolysis, except ZR75-1, which is osteoblastic. Similar to mice with MDA-MB-231 breast cancer bone metastases, mice with osteolytic or mixed osteolytic/osteoblastic (components of bone destruction as well as bone formation) also had lower EDL *ex vivo* muscle specific force compared to non-tumor control mice.

Mice with A549 human lung cancer bone metastases had osteolytic bone destruction, reduced forelimb grip strength and lower *ex vivo* muscle specific force generation of the EDL than non-tumor control mice (**Supplementary Fig. 2a**). Similar to MDA-MB-231 breast cancer bone metastases, A549 caused lower muscle weights (EDL, tibialis anterior, soleus, and gastrocnemius) and reduced body weight due to loss of both lean and fat mass compared to non-tumor control mice (**Supplementary Fig. 2b**). Skeletal muscle RyR1 channels from mice with A549 lung cancer bone metastases also exhibited the biochemical signature of leaky channels[10,13] as those observed in skeletal muscle from MDA-MB-231 mice (**Supplementary Fig. 2c**). RWGT2 human lung cancer bone metastases[15] caused mixed osteolytic/osteoblastic lesions in bone and had lower *ex vivo* muscle specific force of

the EDL without reduced forelimb grip strength compared to non-tumor control mice (**Supplementary Fig. 2d**). RWGT2 did not lower skeletal muscle weight (with the exception of the soleus), reduce whole body weight, alter body composition or cause lower mid-calf cross-sectional area compared to non-tumor control mice (**Supplementary Fig. 2e**). Mice with RWGT2 lung cancer bone metastases did exhibit RyR1 modifications similar to MDA-MB-231 breast cancer bone metastases (**Supplementary Fig. 2f**).

MCF-7 breast cancer-associated bone metastases, which has components of bone destruction and bone formation (mixed osteolytic/osteoblastic) also had lower *ex vivo* muscle specific force of the EDL compared to non-tumor control mice (**Supplementary Fig. 2g**). Mice with MCF-7-associated bone metastases did not have lower muscle weight but did lose total body weight compared to non-tumor control animals (**Supplementary Fig. 2h**). Skeletal muscle RyR1 channels from mice with MCF-7 breast cancer and bone metastases also exhibited the same biochemical signature of leaky channels as observed in MDA-MB-231 tumor bearing mice with bone metastases (**Supplementary Fig. 2i**).

PC-3 human prostate cancer caused osteolytic metastases and reduction in forelimb grip strength and lower *ex vivo* muscle specific force of the EDL in tumor-bearing mice compared to non-tumor control mice (**Supplementary Fig. 3a**). These mice also had lower muscle weight, reduced body weight and fat and lean mass compared to non-tumor control animals (**Supplementary Fig. 3b**) and the biochemical signature of leaky RyR1 channels compared to non-tumor control mice (**Supplementary Fig. 3c**).

Direct inoculation of human JJN3 multiple myeloma cells into the tibia caused bone destruction as previously described[16] but no loss of body weight. Mice with JJN-3 multiple myeloma had lower *ex vivo* muscle specific force of the EDL measured in the contralateral limb and RyR1 channels exhibited the biochemical signature of leaky channels compared to non-tumor control mice (**Supplementary Fig. 3d**). JJN-3 multiple myeloma-induced bone destruction (osteolytic lesion area) correlated with decreased specific force of the EDL in the contralateral limb (without decreased muscle mass or body weight) compared to non-tumor control mice, indicating once again that local bone destruction in the tumor-bone microenvironment can cause systemic muscle weakness (**Supplementary Fig. 3e**).

In contrast, mice with the human breast cancer, ZR75-1, had bone metastases with abnormal new bone formation without bone destruction (osteoblastic) and lower *ex vivo* muscle specific force of the EDL but not reduced forelimb grip strength compared to non-tumor control mice (**Supplementary Fig. 3f**). There was no loss of muscle weight or whole body weight nor did the mice have body composition changes, although mid-calf cross-sectional area was higher compared to non-tumor control mice (**Supplementary Fig. 3g**). RyR1 modifications were not observed (**Supplementary Fig. 3h**).

Taken together these data show that predominantly osteolytic (MDA-MB-231 breast cancer, A549 lung cancer, PC3 prostate cancer, JJN3 multiple myeloma) or mixed osteolytic/ osteoblastic bone metastases (RWGT2 lung cancer and MCF-7 breast cancer) result in lower muscle specific force production, lower muscle strength and RyR1 modifications that are consistent with leaky channels, regardless of whether there was weight loss or lower muscle

mass compared to non-tumor control mice. On the other hand, ZR75-1 breast cancer induces osteoblastic bone metastases and lower muscle function but no modification of RyR1 compared to non-tumor control mice. Notably it takes seven months for the ZR75-1 mice to develop bone metastases and muscle weakness as opposed to 4–12 weeks for all of the other models we examined. The lower muscle force production in the ZR75-1 mice occurs in the absence of bone destruction and without RyR1 modifications suggesting a mechanism distinct from the other forms of cancer in bone.

Inhibiting RyR1 Ca^{2+} leak improves muscle strength

The clinical relevance of the leaky RyR1 modifications in skeletal muscle from mice with osteolytic bone metastases is reinforced because the same biochemical signature of leaky RyR1 channels is found in skeletal muscle from humans with osteolytic breast or lung cancer metastatic to bone (**Fig. 1e–f**). The RyR1 Ca^{2+} release channel stabilizer Rycal (S107) is a small molecule in the 1,4-benzothizepine family whose structure and properties have been previously published[17]. S107 fixes leaky RyR1 channels by inhibiting oxidation-induced depletion of the channel stabilizing subunit calstabin1 from the RyR1 complex which stabilizes the closed state of the channel and prevents aberrant intracellular Ca^{2+} leak, improving the Ca^{2+} signal for muscle force production and enhancing muscle strength and exercise capacity in rodents[10,13,17,18]. S107 (via subcutaneous infusion pump to achieve a plasma level of 252 ± 75.1 nM; s.e.m., $n = 10$) improved forelimb grip strength and *ex vivo* muscle specific force of the EDL in mice with breast cancer-associated bone metastases compared to vehicle treated mice (**Fig. 2a–b**). S107 prevented depletion of calstabin1 from the skeletal muscle RyR1 complex in mice with bone metastases but, as previously reported, did not prevent oxidation or nitrosylation of RyR1[10,13] compared to vehicle treated mice (**Fig. 2c**). S107 treatment led to higher peak tetanic Ca^{2+} in muscle fibers (**Fig. 2d**), and lower skeletal muscle RyR1 open probability (P_o) (**Fig. 2e**) consistent with decreased SR Ca^{2+} leak compared to vehicle treated mice. The SR/ER Ca^{2+} ATPase (SERCA) pumps Ca^{2+} back into the SR and lower SERCA activity could contribute to decreased tetanic Ca^{2+}, but we observed no difference in SERCA activity in skeletal muscle from non-tumor mice compared to mice with bone metastases either with or without S107 (**Fig. 2f**).

S107 had no effect on the development and progression of bone metastases, tumor burden, the number of osteoclasts present at the tumor bone interface (**Supplementary Fig. 4a**), body weight, or the distribution of fat and lean mass compared to vehicle treated mice (**Supplementary Fig. 4b**). S107 did not improve muscle mass, affect muscle fiber diameter or mid-calf cross-sectional area compared to vehicle treated mice (**Supplementary Fig. 4c**). However, S107 treatment did eliminate the correlation between higher bone destruction and lower muscle function (**Fig. 2g**).

Calorie restriction by reducing food intake (**Supplementary Fig. 4d**) in healthy mice for two weeks led to reduced body weight and fat and lean mass and led to lower muscle weight and mid-calf cross-sectional area compared to pair-fed mice (**Supplementary Fig. 4e**). Grip strength and *ex vivo* contractility of the EDL muscle was not affected by reduced calorie intake (**Supplementary Fig. 4f**). This shows that loss of muscle mass alone does not account for lower strength in mice with bone metastases.

Inhibiting TGF-β improves muscle strength

Bone is the largest source of TGF-β in the body[19] and TGF-β which is deposited in bone matrix by osteoblasts, plays a central role in tumor growth in bone[6,7,20,21]. TGF-β is released from mineralized bone matrix during osteoclastic resorption. This resorbing bone matrix is the primary source of TGF-β activity in mice with MDA-MB-231 bone metastases; bisphosphonate inhibition of osteoclastic bone resorption inhibit TGF-β signaling in these bone metastases[7,19]. TGF-β-induced SMAD3 phosphorylation[22] was higher in skeletal muscle from mice with MDA-MB-231 breast cancer bone metastases compared to non-tumor control mice (**Fig. 3a**), but not in mice with MDA-MB-231 primary tumors without bone metastases (**Supplementary Fig. 5a**) consistent with a systemic effect of bone-derived TGF-β on skeletal muscle. The clinical relevance of the activation of TGF-β mediated signaling in skeletal muscle in the presence of cancer-induced bone destruction was reinforced because SMAD3 phosphorylation was also higher in skeletal muscle from humans with breast cancer bone metastases (**Fig. 3b**) and in humans with lung cancer bone metastases compared to humans without bone metastases (**Fig. 3c**). Serum TGF-β concentrations were higher in tumor-bearing mice with bone metastases, but not in those with primary breast cancer compared to non-tumor mice (**Fig. 3d**). Skeletal muscle from five additional mouse models of human cancers with osteolytic or mixed osteolytic/osteoblastic bone metastases due to A549 lung cancer, RWGT2 lung cancer, MCF-7 breast cancer, PC-3 prostate cancer, and JJN-3 multiple myeloma all showed higher SMAD3 phosphorylation consistent with activation of TGF-β-mediated signaling in skeletal muscle compared to non-tumor control mice (**Supplementary Fig. 5a**). In contrast, the osteoblastic ZR75-1 breast cancer bone metastases did not exhibit higher SMAD3 phosphorylation in skeletal muscle compared to non-tumor control mice (**Supplementary Fig. 5a**).

Next we showed that inhibition of TGF-β improves muscle strength by treating mice with MDA-MB-231 bone metastases with: 1) the TGF-β receptor I kinase inhibitor SD-208 (60 mg/kg daily gavage); 2) bisphosphonate (zoledronic acid [ZA]) (5 μg/kg 3/week SC injection), which specifically inhibits osteoclastic bone resorption and lowers TGF-β release from the bone matrix[7]; 3) combined therapy (SD-208 + ZA); or 4) a pan-TGF-β neutralizing antibody (clone 1D11)[23]. Serum TGF-β concentrations were decreased in MDA-MB-231 tumor bearing mice with bone metastases treated with ZA as a consequence of lower release of TGF-β from the bone compared to vehicle treated mice (**Fig. 3d**). Bone metastases-bearing mice treated with SD-208, ZA or the combination all had lower skeletal muscle SMAD3 phosphorylation compared to vehicle treated mice, indicating inhibition of TGF-β signaling (**Fig. 3e**). Both SD-208 and ZA treatment, alone and in combination, improved muscle function (forelimb grip strength and muscle specific force of the EDL) (**Fig. 3f–g**), RyR1 oxidation and nitrosylation and preserved calstabin1 binding to the RyR1 complex compared to vehicle treated mice (**Fig. 3h**). The activity of SERCA was not affected by treatment with SD-208, ZA or combined therapy compared to vehicle treated mice (**Supplementary Fig. 5b**). *In vitro*, SD-208 blocked TGF-β-induced SMAD3 phosphorylation in C2C12 myotubes (**Supplementary Fig. 5c**). Taken together these data show that bone-derived TGF-β plays a key role in lower muscle specific force production and cancer-associated muscle weakness possibly via oxidation of RyR1.

SD-208 or ZA prevented loss of skeletal muscle, body weight and lower mid-calf cross-sectional area in mice with bone metastases and the combined therapy (SD-208 + ZA) provided additive benefit (**Supplementary Fig. 5d–g**), lower tumor burden (**Supplementary Fig. 5h**) and lower number of osteoclasts at the tumor-bone interface compared to vehicle treated mice (**Supplementary Fig. 5i**).

Since SD-208 is a TGF-β receptor I kinase inhibitor it may also inhibit the effects of other TGF-β family members, including activin and myostatin. To determine the specificity of TGF-β to induce muscle weakness we treated mice with breast cancer bone metastases with a pan-TGF-β neutralizing antibody (clone 1D11)[23], or isotype control (10 mg/kg 3 times per week, i.p. injection)[24]. The TGF-β neutralizing 1D11 antibody has no effect on activin or myostatin signaling[23]. Mice with MDA-MB-231 breast cancer bone metastases treated with 1D11 antibody showed lower SMAD3 phosphorylation (**Fig. 4a**), increased forelimb grip strength and higher *ex vivo* specific force generation of the EDL muscle (**Fig. 4b–c**), lower RyR1 oxidation and nitrosylation and higher binding of calstabin1 to the RyR1 complex consistent with fixing the leaky RyR1 channels compared to isotype antibody treated control mice (**Fig. 4d**). 1D11 lowered SMAD3 phosphorylation in TGF-β-treated C2C12 myotubes compared to control treated cells (**Supplementary Fig. 6a**). 1D11 treated mice showed higher hindlimb muscle weight, increased body weight (due to increases in both fat and lean content) and higher mid-calf cross-sectional area compared to isotype antibody treated control mice (**Supplementary Fig. 6b–e**). Mice treated with 1D11 had lower bone destruction (osteolytic lesion area of limbs) (**Supplementary Fig. 6f–g**), lower tumor burden, and there was no effect on the number of osteoclasts at the tumor-bone interface compared to isotype antibody treated control mice (**Supplementary Fig. 6h–i**). Taken together these data indicate that TGF-β inhibition improves muscle function and that bone-derived TGF-β contributes to cancer-associated muscle weakness, at least in part, by inducing oxidation of RyR1.

To directly show that TGF-β is sufficient to cause RyR1 channel remodeling and intracellular Ca^{2+} leak we treated differentiated C2C12 myotubes with TGF-β. TGF-β treatment induced the biochemical signature of leaky RyR1. Binding of calstabin1 to RyR1 (which fixes the RyR1 mediated leak) was restored by incubation of myotubes with S107 compared to C2C12 myotubes without TGF-β treatment (**Fig. 4e**). TGF-β increased Ca^{2+} sparks in myotubes (a direct measure of RyR1 mediated SR Ca^{2+} leak), and increased Ca^{2+} sparks were prevented by S107 compared to C2C12 myotubes without TGF-β treatment (**Fig. 4f**). Thus, TGF-β activates a signaling pathway that leads to RyR1 oxidation, SR Ca^{2+} leak in skeletal muscle cells.

RyR1 oxidation is mediated by Nox4

We next sought to determine the mechanisms by which TGF-β mediates oxidation of RyR1. Nox4 is a membrane protein that transfers electrons from NADPH to O_2 to form reactive oxygen species (ROS), which oxidize many molecules including proteins. Nox4 is expressed in skeletal muscle including in the SR where it interacts with RyR1 resulting in its oxidation[25]. TGF-β leads to higher expression of Nox4[26-29]. We found that skeletal muscle from mice with bone metastases had 3-fold higher *Nox4* mRNA and S107 had no effect on

Nox4 expression compared to non-tumor control mice (**Fig. 5a**). SD-208, ZA, SD-208 + ZA and 1D11 antibody all lowered skeletal muscle *Nox4* mRNA expression compared to appropriate vehicle treated control mice (**Fig. 5a**) (*Nox1* and *Nox2* mRNA were not altered in mice with MDA-MB-231 bone metastases compared to non-tumor control mice, **Supplementary Fig. 7a**). Moreover, total protein oxidation (measured as carbonyl concentration in skeletal muscle lysates as described in the Online Methods) was higher in skeletal muscle from mice and humans with cancer and bone metastases compared to mice and humans without bone metastases and inhibiting TGF-β signaling lowered protein oxidation in mice with bone metastases compared to vehicle treated mice (**Fig. 5b**). Indeed, total protein oxidation (carbonyl concentration) was higher in skeletal muscle from all bone metastases models associated with bone destruction, but not in skeletal muscle from mice with primary MDA-MB-231 breast cancer without bone metastases or those with osteoblastic ZR-75-1 bone metastases compared to non-tumor control mice. These data indicate that tumor-induced bone destruction is associated with oxidation of skeletal muscle. Moreover, inhibiting TGF-β release, or signaling, or blocking Nox4 all lowered the carbonyl concentration in skeletal muscle lysates from mice with tumors metastatic to bone (**Supplemental Table 3**) indicating the importance of TGF-β-Nox4 in the oxidation of skeletal muscle proteins in the setting of tumors metastatic to bone.

Nox4 co-immunoprecipitated with RyR1 in skeletal muscle from mice with MDA-MB-231 breast cancer bone metastases compared to non-tumor control mice (**Fig. 5c**) as well as in skeletal muscle samples from humans with breast cancer bone metastases or humans with lung cancer bone metastases compared to humans without bone metastases (**Fig. 5d–e**). The amount of Nox4 co-immunoprecipitating with RyR1 was higher in muscle from mice with breast cancer bone metastases (**Fig. 5c** and **Supplementary Fig. 7b**), humans with breast cancer bone metastases (**Fig. 5d**), in mice with lung cancer bone metastases (**Supplementary Fig. 7b**), humans with lung cancer bone metastases (**Fig. 5e**), in mice with PC-3 prostate cancer, and in mice with JJN-3 multiple myeloma compared to non-tumor controls. Mice with MDA-MB-231 primary breast cancer without bone metastases, or in mice with ZR75-1 osteoblastic breast cancer bone metastases that were not associated with RyR1 oxidation did not have higher RyR1-Nox4 co-immunoprecipitation compared to non-tumor control mice (**Supplementary Fig. 7b**).

TGF-β-mediated higher Nox4 protein expression in C2C12 myotubes compared to C2C12 myotubes without TGF-β treatment and was blocked by SD-208 but not S107 (**Fig. 5f–g**). TGF-β let to higher Nox4 co-immunoprecipitation with RyR1 channels in myotubes (**Fig. 5h**). Moreover, *Nox4* knock-down in myotubes prevented TGF-β-induced RyR1 oxidation and loss of calstabin1 binding to RyR1 (**Fig. 5i**) and prevented TGF-β-induced ROS production compared to C2C12 myotubes without TGF-β treatment (**Fig. 5j**).

To test the *in vivo* effect of Nox4 inhibition, we treated mice with MDA-MB-231 breast cancer bone metastases with the Nox1/Nox4 inhibitor GKT137831[30] [60 mg/kg/day or vehicle (1.2% methylcellulose + 0.1% Polysorbate 80), administered by daily oral gavage]. GKT137831 prevented skeletal muscle oxidation and nitrosylation of RyR1, restored calstabin binding (**Fig. 6a**), and improved EDL muscle-specific force (**Fig. 6b**) in mice with MDA-MB-231 bone metastases compared to vehicle treated mice. GKT137831 had no

effect on the amount of skeletal muscle Nox4 associated with RyR1 (**Fig. 6c**) and did not block upstream TGF-β signaling as skeletal muscle SMAD3 phosphorylation was not affected compared to vehicle treated mice (**Fig. 6d**). In mice with bone metastases, GKT137831 had no effect on osteolytic lesion size, muscle mass, body weight, body composition, or grip strength (compared to vehicle treated mice) likely reflecting the high variability of the latter measurement which also has a behavioral component (**Supplementary Fig. 7c–h**).

No contribution by non-bone sites or fibrosis to weakness

The tumor-bone microenvironment appears to be the most significant determinant of muscle weakness in this model, since the bisphosphonate zoledronic acid prevented oxidation of RyR1 and muscle weakness by blocking release of TGF-β from bone. Consistent with this, tumor burden at other metastatic sites was insignificant. In mice with MDA-MB-231 breast cancer and bone metastases, the tumor burden in bone was at least 12-fold higher than in all other organs (**Supplementary Fig. 8a**). Further, there was no evidence of skeletal muscle fibrosis (**Supplementary Fig. 8b**), supporting the finding that muscle weakness is due to tumor-induced bone destruction.

To validate the role that higher bone resorption plays in skeletal muscle weakness in the absence of cancer, we tested a mouse model of CED. This disease is an inherited human skeletal disease characterized by increased bone destruction and skeletal fragility that is often associated with TGF-β1 mutations that cause an increase TGF-β activity by increased activation or secretion of TGF-β[31,32]. In the mouse model of CED, a mutant TGF-β1 (H222D), identified from some humans with CED, is expressed under the control of the 2.3-kb type I collagen promoter. Mice show higher bone destruction and fractures which is abrogated by TGF-β signaling blockade, using a TGF-β receptor I inhibitor. CED mice show higher concentrations of active TGF-β in the bone microenvironment and higher bone resorption compared to littermate controls[8]. Radiography of the lower hindlimb of CED mice showed osteolysis and diaphyseal dysplasia similar to previous reports compared to littermate controls[8] (**Supplementary Fig. 8c**). Consistent with higher TGF-β signaling, skeletal muscle from CED mice had higher SMAD3 phosphorylation compared to littermate control mice (**Supplementary Fig. 8d**). CED mice also had lower *ex vivo* specific force of the EDL muscle compared to non-affected littermate control mice (**Supplementary Fig. 8e**), consistent with previous reports in which treatment of mice with recombinant TGF-β that resulted in lower skeletal muscle specific force[33]. Skeletal muscle from CED mice also showed higher levels of RyR1 oxidation and nitrosylation, lower amounts of calstabin1 bind bound to RyR1 and higher levels of Nox4-RyR1 binding compared to littermate control mice (**Supplementary Fig. 8f**). These results were similar to those we observed in mice with osteolytic bone metastases.

Taken together our data in models of osteolytic bone metastases show that TGF-β, released from the bone matrix due to elevated catabolism of the tissue, upregulates *Nox4*, and causes higher association of Nox4 protein with RyR1 resulting in oxidation of the channel. RyR1 oxidation causes an SR Ca^{2+} leak that lowers tetanic Ca^{2+}, impairs muscle force production, and contributes to muscle weakness in cancer with bone metastases (**Fig. 6e**). Similar

skeletal muscle dysfunction, higher skeletal muscle TGF-β activity and RyR1 oxidation via upregulation of Nox4 were observed in a non-malignant bone disorder associated with increased bone destruction (CED mice).

DISCUSSION

The present study provides novel mechanistic insights into the causes of cancer-associated muscle weakness with potential therapeutic implications for the following reasons: 1) in addition to loss of muscle mass we now show that there is a specific loss of muscle function in the setting of bone metastases and that muscle weakness can occur without the loss of muscle mass; 2) an important determinant of muscle weakness in metastatic cancer is bone destruction; 3) a key mediator of muscle weakness is TGF-β released from bone as a consequence of tumor-induced osteoclast activity in the tumor-bone microenvironment; 4) TGF-β activates Nox4 in skeletal muscle causing protein oxidation; 5) skeletal muscle RyR1 Ca^{2+} release channels are a target of the oxidative stress resulting from upregulation of Nox4 by TGF-β; 6) RyR1 oxidation results in intracellular Ca^{2+} leak that lowers tetanic Ca^{2+} and weakens muscle force production; 7) activation of TGF-β signaling, upregulation of Nox4, and the biochemical signature of oxidation-induced skeletal muscle RyR1 leak were all present in humans with breast or lung cancer metastatic to bone and in six out of seven mouse models of human osteolytic bone including breast, lung and prostate cancers, as well as multiple myeloma; 8) inhibition of RyR1-mediated SR Ca^{2+} leak, inhibition of TGF-β activity, inhibition of TGF-β release from bone, or inhibition of Nox4 all improved muscle force production suggesting multiple potential therapeutic targets for cancer associated muscle weakness in the setting of bone destruction due to metastases. Furthermore, this mechanism of muscle weakness was also observed in a non-malignant bone disorder characterized by increased bone destruction and TGF-β activity. Thus, targeting skeletal muscle weakness caused by the TGF-β-Nox4-RyR1 axis represents a novel therapeutic approach to improve quality of life in patients with muscle weakness associated with increased bone destruction.

In addition to RyR1, other proteins involved in muscle contraction were oxidized in skeletal muscle from mice with bone metastases suggesting that there may be other contributing factors to cancer-associated muscle weakness. Inhibition of the activin receptor reduced cachexia and cardiac atrophy and improved survival in mice with experimental colon cancer cachexia (C26 model)[34]. Another target under investigation for cachexia is myostatin, a negative regulator of muscle mass[35]. Myostatin antagonism with anti-myostatin antibody improved contractile properties of dystrophic muscle using the *mdx* mouse model of Duchenne muscular dystrophy[36]. However, myostatin deficient mice showed a decrease in muscle contractile force that is age-, sex-, and muscle-dependent[2,3]. Our data do not exclude the possibility that other bone-derived factor(s) released as a consequence of osteoclastic bone resorption may induce TGF-β production from other sources, or may themselves contribute to skeletal muscle dysfunction or loss of muscle mass. Furthermore, the data do not indicate that the mechanism described herein is the exclusive mechanism for cancer-associated muscle weakness, but rather is one such mechanism in humans with bone metastases.

Taken together our data provide a link between bone and skeletal muscle by showing that factors elaborated from bone can profoundly affect muscle function systemically. Our findings in mouse models of breast cancer, lung cancer, prostate cancer and multiple myeloma, and in humans with breast cancer- or lung cancer-associated with bone destruction suggest a generalized, but not exclusive role, for the tumor-bone microenvironment in the generation of cancer-associated skeletal muscle weakness. Finally, the data indicate that muscle dysfunction can occur prior to the loss of muscle mass (cachexia) and suggest that a spectrum of muscle dysfunction exists ranging from muscle weakness to profound cachexia in humans with bone metastases. Indeed, muscle weakness may occur in states of increased bone destruction, even in the absence of cancer. Clinical studies to characterize this spectrum of muscle dysfunction are justified in order to develop and test treatment to prevent muscle weakness associated with cancer as well as associated bone disorders.

ONLINE METHODS

Animals

Female athymic nude mice were obtained from Harlan (Indianapolis, IN) and female CB.17 SCID mice were obtained from Charles River (Hollister, CA) at 5 weeks of age. Camurati-Engelmann disease (CED) mice previously described and were provided by Xu Cao, Johns Hopkins (Baltimore, MD)[8]. 6-week-old male CED and littermate control animals were used for experiments. All experiments with animals were performed at Indiana University and approved by Indiana University's Institutional Animal Care and Use Committee (IACUC). Each animal experiment was performed once unless otherwise stated.

Ethics statement

In all studies, mice were handled and euthanized in accordance with approved institutional, national and international guidelines.

Materials

Recombinant human TGF-β1 was purchased from R&D Systems. SD-208 was obtained from Epichem Pty Ltd (Bentley, WA). Zoledronic acid (Zometa) was obtained from Novartis (Cambridge, MA). Rycal S107 (S107-HCl, FW 245.77) was synthesized as previously described[17,37]. Anti-TGF-β antibody clone 1D11.16.8 (1D11) and mouse IgG1 isotype control (MOPC-21; unknown specificity) were obtained from BioXCell (West Lebanon, NH). Nox4 inhibitor (GKT137831) was obtained from Ark Pharm, Inc. (Libertyville, IL). Antibodies: Anti-RyR (Affinity Bioreagents, cat. MA3-916, Golden, CO; 1:2,000), anti-Cys NO antibody (Sigma, cat. N0409, St. Louis, MO; 1:2,000), anti-calstabin antibody (Santa Cruz Biotechnology, cat. sc-6173, Santa Cruz, CA; 1:2,500), anti-DNP (Oxyblot, Millipore, Darmstadt, Germany; 1:250), anti-pSMAD3 (Abcam, cat. ab40854, Cambridge, UK; 1:1000), anti-SMAD3 (Abcam, cat. 52903, Cambridge, UK; 1:1000), anti-Nox4 (Abcam, cat. 109225, Cambridge, UK; 1:1000), anti-GAPDH (Sigma, cat. G8795, St. Louis, MO; 1:500) and anti-tubulin (Sigma, cat. 8203, St. Louis, MO; 1:500 each). Fluo-4 AM and Fura-red were obtained from Invitrogen/Molecular probes (cat. F-14201 and cat. F-3020, Eugene, OR).

Cell culture

MDA-MB-231 breast cancer cells[38] (HTB-26, ATCC, Manassas, VA), MCF-7 breast cancer cells[39] (HTB-22, ATCC), ZR75-1 breast cancer cells[40] (CRL-1500, ATCC), PC-3 prostate cancer cells[41] (CRL-1435, ATCC), and RWGT2 lung cancer cells[15,42] (isolated from bone metastases by Dr. Guise as reported[15]) were cultured in Dulbecco's modified Eagle's media (DMEM) (Hyclone, Logan, UT) containing 10% heat-inactivated fetal bovine serum (FBS) (Hyclone). JJN-3 multiple myeloma cells[43] (ACC 541, DSMZ) were cultured in RPMI 1640 (Invitrogen, Grand Island, NY) containing 10% heat-inactivated FBS. A549 cancer cells (CCL-185, ATCC) were cultured in 1640 RPMI (Hyclone) containing 10% heat-inactivated FBS. C2C12 myoblast cells (CRL-1772, ATCC) were cultured subconfluently in DMEM containing 10% heat-inactivated FBS. C2C12 myoblasts were differentiated into myotubes by culture in DMEM containing 2% heat-inactivated horse serum (HS) (Hyclone). All cells were maintained at 37° C with 5% CO_2 in a humidified chamber. All cells were verified to be free of mycoplasma contamination via routine PCR testing. No independent verification was completed. Cells treated with recombinant human TGF-β1 (R&D Systems, Minneapolis, MN) were starved in DMEM (no serum) for 16-20 hrs and 5 ng/ml TGF-β1 was added to cells in DMEM.

In vivo models

Intracardiac inoculation of tumor cells was performed as previously described[11,38] into four-week old female athymic nude mice. Tumor cells (MDA-MB-231 and A549) were trypsinized, washed twice and resuspended in PBS to a final concentration of 10^5 cells in 100 μl. 100,000 cells were inoculated into each animal. Animals were anesthetized with ketamine/xylazine and positioned ventral side up. MDA-MB-231 or A549 cells were inoculated into the left ventricle by percutaneous injection using a 26-gauge needle. Visualization of bright red blood entering the hub of the needle in a pulsatile fashion indicated a correct position in the left cardiac ventricle. Animals were sacrificed at four-weeks post-inoculation.

Mammary fat pad tumor inoculation was performed on four-week old female athymic nude mice. Tumor cells (MDA-MB-231) were trypsinized, washed twice and resuspended in PBS to a final concentration of 10^6 cells in 100 μl. 1,000,000 cells were inoculated into each animal. Mice were anaesthetized with ketamine/xylazine and inoculated in the upper mammary fat pad using a 27-gauge needle. Animals were sacrificed at four-weeks post-inoculation.

Intra-tibial inoculation of tumor cells was performed on four-week old female CB.17 SCID mice. Tumor cells (JJN-3) were trypsinized, washed twice and resuspended in PBS to a final concentration of 10^5 cells in 20 μl. 100,000 cells were inoculated into each animal. Mice were anaesthetized with ketamine/xylazine and inoculated in the proximal tibia using a 27-gauge needle. Animals were sacrificed at 34-days post-inoculation.

Radiography

Osteolytic lesions were analyzed by radiography using a Kubtec digital X-ray imager (Kubtec, Milford, CT). Mice were imaged in a prone position at 2.7× magnification.

Osteolytic lesion area was quantified using BioQuant software v14.1.6 (Bioquant Image Analysis Corporation, Nashville, TN). The investigators were blinded to treatment of subjects.

Bone histology and histomorphometry

Forelimbs, hindlimbs, and spine of the mice were collected upon euthanasia and fixed in 10% neutral buffered formalin for 48 h and decalcified in 10% EDTA for 2 weeks. After decalcification tissues were processed in a Shandon Excelsior automated tissue processor (Thermo Fisher Scientific, Grand Island, NY) and embedded in paraffin wax for sectioning. Longitudinal, mid-sagittal sections 3.5 μm in thickness from the tibia, femur, humerus and lumbar spines were cut using an automated Microm HM 355 S microtome (Thermo Fisher Scientific). Tissue sections were stained with hematoxylin and eosin (H&E) and prepared for histomorphometric analysis. All section are viewed on Leica DM2500 compound microscope (W. Nuhsbaum Inc., McHenry, IL) with Q-imaging micropublisher cooled CCD color digital camera. Images were captured and analyzed using BioQuant software v14.1.6 (Bioquant Image Analysis Corporation). Tumor burden per mouse, defined as area of bone occupied by the cancer cells, was calculated at the tibia, femur and humerus at 50x magnification on H&E stained sections, as previously described[38]. Osteoclast number at the tumor-bone interface (OCL/mm bone surface) in the femur, tibia and humerus was measured on TRAP stained slides at 200× magnification. The investigators were blinded to treatment of subjects.

Dual energy X-ray absorptiometry

Body composition was determined using a PIXImus mouse densitometer (GE Lunar II, Faxitron Corp., Tucson, AZ). The densitometer was calibrated with a plastic embedded mouse phantom before use. Mice were anesthetized, placed on an adhesive tray in a prone position with limbs spread. Total body measurement was performed excluding the calvarium, mandible and teeth. Values were expressed as percentage change over baseline scan. The investigators were blinded to treatment of subjects.

Micro-computed tomography measurement of cross sectional muscle area (muscle method)

Mouse legs from control and tumor-inoculated mice were scanned using a VIVACT40 (SCANCO Medical AG, Wayne, PA) to measure muscle cross sectional area. Both the tumor inoculated and the contralateral legs were scanned starting at the level of the tibio-fibular joint for 4-5 mm length under general inhalation anesthesia. Scanning parameters of 45 kVp, 133 μA and 620 ms integration time were used as a standard setting to optimize the contrast between muscle and fat tissue. Lower muscle cross sectional area was reported as the difference between the inoculated versus the contralateral control. The investigators were blinded to treatment of subjects.

Micro-computed tomography (bone method)

microCT imaging was performed on the distal femur and the proximal tibia using a VIVACT-40 (Scanco Medical AG). Scans were acquired using a 17.5 μm^3 isotropic voxel

size, 55 kVp peak X-ray tube potential, 200 ms integration time, and were subjected to Gaussian filtration. Total bone volume and bone volume fraction (BV/TV) were evaluated at the distal epiphysis and metaphysis of the femur in a region that spanned 3.5 mm, and at the proximal epiphysis and metaphysis of the tibia in a region that spanned 2.8 mm. A threshold of 160 was used to manually delineate bone from surrounding soft tissue. The investigators were blinded to treatment of subjects.

Grip strength

Forelimb grip strength was assessed by allowing each mouse to grab a wire mesh attached to a force transducer (Bioseb, Vitrolles, France) that records the peak force generated as the mouse is pulled by the tail horizontally away from the mesh[13,44]. We performed three consecutive pulls separated by 5 sec pauses between each pull. We calculated the absolute grip strength (in grams) as the average of the peak forces recorded from the three pulls. The investigators were blinded to treatment of subjects.

Muscle function

Ex vivo contractility of the extensor digitorum longus (EDL) muscles was determined as previously described[10,44]. EDL were dissected from hind limbs and stainless steel hooks were tied to the tendons of the muscles using 4-0 silk sutures and the muscles were mounted between a force transducer (Aurora Scientific, Aurora, ON, Canada) and an adjustable hook. The muscles were immersed in a stimulation chamber containing O_2/CO_2 (95/5%) bubbled Tyrode solution (121 mM NaCl, 5.0 mM KCl, 1.8 mM $CaCl_2$, 0.5 mM $MgCl_2$, 0.4 mM NaH_2PO_4, 24 mM $NaHCO_3$, 0.1 mM EDTA, 5.5 mM glucose). The muscle was stimulated to contract using a supramaximal stimulus between two platinum electrodes. Data was collected via Dynamic Muscle Control/Data Acquisition (DMC) and Dynamic Muscle Control Data Analysis (DMA) programs (Aurora Scientific). At the start of each experiment the muscle length was adjusted to yield the maximum force. The force–frequency relationships were determined by triggering contraction using incremental stimulation frequencies (0.5 ms pulses at 1–150 Hz for 350 ms at supramaximal voltage). Between stimulations the muscle was allowed to rest for 3 min. At the end of the force measurement, the length (L_0) and weight of the muscle was measured and the muscle was snap frozen in liquid N_2. To quantify the specific force, the absolute force was normalized to the muscle size, specifically cross-sectional area, calculated as the muscle weight divided by the length using a muscle density constant of 1.056 kg/m^{-3} [45]. The investigators were blinded to treatment of subjects.

Ca^{2+} imaging in muscle fibers

Single flexor digitorum brevis (FDB) fibers were isolated by enzymatic dissociation as previously described[46]. FDB muscles from the hind limb were incubated for 2 h at 37° C in Dulbecco's Modified Eagles Medium (DMEM) containing 0.3% collagenase 1 (Sigma) and 10% fetal bovine serum. The muscles were transferred to fresh DMEM and gently triturated using a 1000μL pipette until the muscles were dissociated. The cell suspension was stored in an incubator at 37° C and 5% CO_2 until the start of the experiment. FDB fibers were loaded with the fluorescent Ca^{2+} indicator Fluo-4 AM (5 μM, Invitrogen/Molecular probes) for 15

min in RT. The cells were allowed to attach to a laminin-coated glass cover slip that formed the bottom of a perfusion chamber. The cells were then superfused with tyrode solution (121 mM NaCl, 5.0 mM KCl, 1.8 mM $CaCl_2$, 0.5 mM $MgCl_2$, 0.4 mM NaH_2PO_4, 24 mM $NaHCO_3$, 0.1 mM EDTA, 5.5 mM glucose) bubbled with O_2/CO_2 (95/5%). The fibers were triggered to tetanic contraction using electrical field stimulation (pulses of 0.5 ms at supra-threshold voltage, at 70 Hz for 350 ms) and Fluo-4 fluorescence was monitored using confocal microscopy (Zeiss LSM 5 Live, 40× oil immersion lens, excitation wavelength was 488 nm and the emitted fluorescence was recorded between 495 nm and 525 nm) in linescan mode. Only cells that were firmly attached to the glass bottom dish throughout the tetanic stimulation were included in the analysis. After subtraction of background fluorescence, the change in fluorescent signal during the tetanus (peak–resting (ΔF)) was divided by the resting signal ($\Delta F/F_0$). All experiments were performed at RT (approximately 20° C).

Alternatively, basal Ca^{2+} was measured simultaneously with tetanic Ca^{2+}, for which ratiometric imaging of Fluo-4 (excited at 488 nm and emission collected at 505–530 nm) and Fura-red (Invitrogen/Molecular probes) (excited at 488 nm and emission collected at >650 nm) into cells (*F650/F515*). For this method basal [Ca^{2+}] is shown with tetanic [Ca^{2+}]. The investigators were blinded to treatment of subjects.

Proteomics

Skeletal muscle samples (tibialis anterior) were solubilized by ground glass homogenization and brief sonication in lysis buffer (8 M urea, 10 mM DTT solution freshly prepared). The homogenates were centrifuged at 150,000 × g for 20 min at 4° C to remove insoluble materials. Protein concentration was determined by the Bradford Protein Assay. Protein reduction, alkylation, and tryptic digestion were carried out using a conventional method previously published[47]. The proteolyzed protein samples were injected onto a C18 reversed phase column and analyzed using a Thermo-Finnigan linear ion-trap (LTQ) mass spectrometer coupled with a Surveyor autosampler and MS HPLC system (Thermo-Finnigan). The acquired data were searched against the UniProt mouse protein sequence database containing 55,191 protein sequences (released on April 18, 2012) using SEQUEST (v. 28 rev. 12) algorithms in Bioworks (v. 3.3). Differential and post-translational modification on Cysteine of +29 amu was included to identify the site of nitrosylation (C-NO) or oxidation (C-O3H). Identified peptides and proteins and their modification were validated by PeptideProphet, and ProteinProphet, in the Trans-Proteomic Pipeline (TPP, v. 3.3.0) (http://tools.proteomecenter.org/software.php)[48,49]. Only proteins with probability ≥ 0.9000 and peptides with probability ≥ 0.8000 were reported. Protein quantification was performed using IdentiQuantXL software as described [50].

Measurement of protein oxidation, and ROS production

To determine channel oxidation the carbonyl groups on the protein side chains were derivatized to 2,4-dinitrophenylhydrazone (DNP-hydrazone) by reaction with 2,4-dinitrophenylhydrazine (DNPH) (Oxyblot, Millipore, Darmstadt, Germany). The DNP signal on RyR1 was detected by immunoblotting with an anti-DNP antibody (Millipore, Darmstadt, Germany). Protein carbonyl concentration in tissue lysates was determined using the OxiSelect Protein Carbonyl ELISA Kit (Cell Biolabs, inc., San Diego, CA). Briefly, 0.5

mg of EDL lysate was added to a 96 well protein binding plate, which was incubated overnight at 4° C. After washing the plate three times with PBS, the protein carbonyl groups were derivatized with DNPH for 45 min at room temperature (in the dark). Plates were developed with an anti-DNP antibody followed by a HRP conjugated secondary antibody. Protein carbonyl concentration was determined by comparison with a standard curve of oxidized BSA. ROS production was determined in C2C12 myotubes using the OxiSelect *In Vitro* ROS/RNS Assay kit (Cell Biolabs, Inc.). ROS production was measured using 0.25 mg of cell lysate according to the manufacturers recommendations. For H_2O_2 treated cells, cells were incubated with 1 mM H_2O_2 for 30 min prior to lysis. The investigators were blinded to treatment of subjects.

RyR1 immunoprecipitation and immunoblotting

RyR1 oxidation and nitrosylation and calstabin1 binding was determined as previously described[10]. Extensor digitorum longus (EDL) muscles were isotonically lysed in 0.5 mL of a buffer containing 50 mM Tris–HCl (pH 7.4), 150 mM NaCl, 20 mM NaF, 1.0 mM Na_3VO_4, and protease inhibitors. C2C12 cells were lysed in NP-40 lysis buffer containing 50 mM Tris-HCl (pH 8.0) 150 mM NaCl, 1.0% NP-40 and protease inhibitors. An anti-RyR antibody (4 μg anti-RyR1 antibody 5029[10], a custom antibody against the last 9 amino acids [CRKQYEDQLS; a cysteine was added at the N-terminus] of the rabbit skeletal muscle RYR1) was used to immunoprecipitate RyR1 from 250 μg of tissue homogenate. Samples were incubated with antibody in 0.75 mL of a modified RIPA buffer (50 mM Tris–HCl pH 7.4, 0.9% NaCl, 5.0 mM NaF, 1.0 mM Na_3VO_4, 1% Triton-X100, and protease inhibitors) for 1 h at 4° C. The immune complexes were incubated with protein A sepharose beads (Sigma) overnight at 4° C and the beads were washed twice with modified RIPA buffer. Proteins were separated on 4-12% Bis-Tris gels (Life Technologies) and transferred to nitrocellulose for 1 h at 100 V (Bio-Rad, Hercules, CA). After incubation with blocking solution to prevent non-specific antibody binding, immunoblots were developed with anti-RyR (Affinity Bioreagents, cat. MA3-916, Golden, CO; 1:2,000), and anti-Cys-NO antibody (Sigma, cat. N0409, St. Louis, MO; 1:2,000), or an anti-calstabin antibody (Santa Cruz Biotechnology, cat. sc-6173, Santa Cruz, CA; 1:2,500). Immunoblots were developed and quantified using the Odyssey Infrared Imaging System (LICOR Biosystems, Lincoln, NE) and infrared-labeled secondary antibodies. Detection of pSMAD3, SMAD3, Nox4 (Abcam, Cambridge, UK; 1:1000 each), GAPDH and tubulin (Sigma; 1:500 each) from mouse muscle, human biopsies and C2C12 cells was via lysis in NP-40 buffer and detection and quantification of immobilized proteins either using the Odyssey Infrared Imaging System or GE ImageQuant LAS4000 Imaging System (GE Healthcare Bio-sciences, Pittsburgh, PA). The investigators were blinded to treatment of subjects.

Human samples

Muscle biopsies from humans with breast and lung cancer and non-oncologic controls were obtained with consent under a research exempt waiver (IRB# 1403849213) approved by the institutional review board (IRB) of Indiana University School of Medicine from the clinical research laboratory of Dr. Piero Picci at the Istituto Ortopedico Rizzoli, Bologna, Italy. Control muscle samples were from humans with non-cancer related musculoskeletal conditions. Humans with breast and lung cancer all had bone metastases and had not receive

chemotherapy at the time of tissue collection. Of the breast cancer patients, one also had lung metastases and one had tumor cells in the thyroid. Of the lung cancer patients, one also had cancer in the lymph nodes. This study was conducted under protocol approval from the IRB of Indiana University School of Medicine.

Drug treatments

All drug treatments were initiated 48 hours prior to tumor cell inoculation with the exception of Rycal S107, which was initiated at the time of tumor cell inoculation. **SD-208.** As described, SD-208 is a specific inhibitor of the TGF-β type I receptor [51]. SD-208 (60 mg/kg/d) or vehicle (1% methylcellulose) was administered by daily gavage and continued daily for the duration of each study. **Zoledronic acid.** Zoledronic acid (ZA), an anti-resorptive bisphosphonate with FDA approval for use in humans with bone metastases, or vehicle (PBS) was administered by subcutaneous injection (5 μg/kg) 3 times per week for the duration of each study. **Anti-TGF-β antibody.** Antibody clone 1D11.16.8 (1D11) is a neutralizing antibody to all 3 subtypes of TGF-β (TGF-β-1, -2, -3). 1D11 (10 mg/kg) or isotype control (MOPC-21; 10 mg/kg) was administered by intraperitoneal injection 3 times per week for the duration of each study[24]. **Rycal (S107).** S107 is a benzothiazepine derivative that binds the RyR1 channel and enhances the binding affinity of calstabin1[13]. S107 was administered via osmotic infusion pump (Azlet) for continuous delivery. The mini-pump was implanted subcutaneously and the opening sutured and glued. Wounds were monitored for healing. The **Nox4 inhibitor** (GKT137831) (60 mg/kg/day) or vehicle (1.2% methylcellulose + 0.1% Polysorbate 80) was administered by daily gavage for the duration of the study.

Single channel measurements

Muscles were homogenized using a tissue mizer (Fisher Scientific) at the highest speed for 1 min with 2 volumes of: 20 mM Tris-maleate (pH 7.4), 1 mM EDTA and protease inhibitors (Roche). Homogenate was centrifuged at 4,000 g for 15 min at 4° C and the supernatant was centrifuged at 40,000 × g for 30 min at 4° C. The final pellet, containing the SR fractions, was resuspended and aliquoted in 250 mM sucrose, 10 mM MOPS (pH 7.4), 1 mM EDTA and protease inhibitors. Samples were frozen in liquid nitrogen and stored at −80° C. SR vesicles containing RyR1 were fused to planar lipid bilayers formed by painting a lipid mixture of phosphatidylethanolamine and phosphatidylcholine (Avanti Polar Lipids, Alabaster, AL) in a 3:1 ratio in decane across a 200-μm hole in polysulfonate cups (Warner Instruments, Hamden, CT) separating 2 chambers. The trans chamber (1.0ml), representing the intra-SR (luminal) compartment, was connected to the head stage input of a bilayer voltage clamp amplifier. The cis chamber (1.0 ml), representing the cytoplasmic compartment, was held at virtual ground. Symmetrical solutions used were as follows: 1 mM EGTA, 250 mM Hepes, 125 mM Tris-HCl, 50 mM KCl, 0.64 mM $CaCl_2$ (pH 7.35) as cis solution and 53 mM $Ca(OH)_2$, 50 mM KCl, 250 mM Hepes (pH 7.35) as trans solution. The concentration of free Ca^{2+} in the cis chamber was calculated with WinMaxC program (version 2.50; www.stanford.edu/~cpatton/maxc.html). SR vesicles were added to the cis side and fusion with the lipid bilayer was induced by making the cis side hyperosmotic by the addition of 400–500 mM KCl. After the appearance of potassium and chloride channels, the cis side was perfused with the cis solution. Single-channel currents were recorded at 0

mV by using a Bilayer Clamp BC-525C (Warner Instruments), filtered at 1 kHz using a Low-Pass Bessel Filter 8 Pole (Warner Instruments), and digitized at 4 kHz. All experiments were performed at room temperature (23° C). Data acquisition was performed by using Digidata 1322A and Axoscope 10.1 software (Axon Instruments, Sunnyvale, CA). The recordings were analyzed by using Clampfit 10.1 (Molecular Devices, Sunnyvale, CA) and Origin software (ver. 6.0, Microcal Software). The investigators were blinded to the genotype, age and treatment of the groups. Single-channel currents were measured at 150 nM cytosolic [Ca^{2+}] using Ca^{2+} as a charge carrier at 0 mV. Chanel openings are shown as upward deflections; the closed (c-) state of the channel is indicated by horizontal bars in the beginning of each trace. P_o; open probability, T_o; average open time, T_c; average closed time. The activity of the channel indicated by the thick black bar is shown on the expanded time scale. The investigators were blinded to treatment of subjects.

SERCA activity

SERCA activity was measured using the malachite green procedure for phosphate determination, adapted to the microscale as previously described[52]. The reaction was started by the addition of 50 μg of EDL microsomes to 150 μl of reaction mixture (20 mM MOPS/Tris-HCl, pH 6.8, 100 mM KCl, 5 mM $MgCl_2$, 5 mM ATP, 1 mM EGTA. 0.350 mM $CaCl_2$ (free Ca^{2+} concentration of approximately 500 nM as calculated using the CHELATOR program). After 5 min, the reaction was stopped by the transfer of 120 μl of reaction mixture to 80 μl of malachite green reagent mixture in a 96-well microplate. The malachite green reagent mixture was made by mixing 0.122% malachite green hydrochloride in 6.2 N H_2SO_4, 5.76% ammonium paramolybdate tetrahydrate, and 11% Tween-20 in a volume ratio of 100:66:2. Color development was quenched after 10 s by the addition of 45 μl of 15.1% sodium citrate dihydrate. Inorganic phosphate liberated in the ATPase reaction was quantified by comparison of absorbance at 570 nm with standard curves generated with known amounts of Na_2HPO_4 in the reaction buffer. The investigators were blinded to treatment of subjects.

Enzyme-linked immunosorbent assay (ELISA)

ELISA assay for TGF-β quantification from mouse serum was performed using Quantikine human TGF-β1 (R&D Systems; Minneapolis, MN; USA) according to manufacturer's guidelines. Serum samples were diluted 1:20 in calibrator diluent. ELISA plates were analyzed by absorbance reading using a microplate reader set to 450 nm with wavelength correction set to 540 nm. Investigators were blinded to sample identity.

Caloric restriction

Caloric restriction was determined by measuring food intake in mice with MDA-MB-231 breast cancer bone metastases as an average amount of food in grams (calculated by per cage basis n = 5 mice per cage). Food was restricted to healthy animals (n = 10 per group; strain, age and sex matched to bone metastasis model) for one week following 3 weeks of ad libitum feeding to maintain consistency with previous animal studies. Calculated feedings (30–40% reduction of normal intact) and body weight measurements was completed at the same time each day. The investigators were blinded to treatment of subjects.

Ca^{2+} sparks measurements

C2C12 cells were incubated in a relaxing solution (140 mM K-glutamate, 10 mM HEPES, 10 mM $MgCl_2$, 0.1 mM EGTA, pH 7.0). Cells were permeabilized in relaxing solution containing 0.01% saponin for ~30 s. After washing the sample with a saponin free solution, the solution was changed to an internal medium (140 mM K-glutamate, 5 mM Na_2ATP, 10 mM glucose, 10 mM HEPES, 4.4 mM $MgCl_2$, 1.1 mM EGTA, 0.3 mM $CaCl_2$, Fluo-3 (pentapotassium salt, Invitrogen/Molecular probes, pH 7.0) for Ca^{2+} sparks acquisition as previously reported[13]. Fluorescence images were acquired with a Zeiss LSM 5 Live confocal system (63× oil immersion, NA = 1.4) operated in line-scan mode (x vs. t, 1.5 ms/line, 3000 lines per scan) along the longitudinal axis of the fibers. Each location was scanned at most twice prior to moving the line location. Fluo-3 was excited with an Argon laser at 488 nm, and the emitted fluorescence was recorded between 495–555 nm. Image analysis was performed using custom made routines compiled in IDL (v7.1, ITT). Potential Ca^{2+} spark areas were empirically identified using an autodetection algorithm[53]. The mean F value for the image was calculated by summing and averaging the temporal F at each spatial location while ignoring potential spark areas. This F value was then used to create a $\Delta F/F$ image pixel by pixel. Statistical comparisons were performed using the ANOVA test with a significance level set at $P<0.05$. The investigators were blinded to the treatment of subjects.

Semi-quantitative RT-PCR

Tibialis anterior (TA) muscle was lysed by dounce homogenization in Trizol (Invitrogen) for RNA extraction. One-fifth volume chloroform was added to lysates and vortexed vigorously for 15 sec and incubated at room temperature for 3 min. Samples were centrifuged (12,000 g, 15 min, 4° C) and the upper aqueous phase was collected and loaded onto a GenElute mammalian total RNA mini column (Sigma). Total RNA was isolated according to manufacturer's instructions. DNase I treatment was performed to remove genomic DNA contamination (Qiagen), and RNA integrity was assessed on agarose gels. RNA (500 ng per sample) was reverse transcribed using Superscript II (Invitrogen) according to the manufacturer's instructions with anchored oligo(dT) (Promega) for priming. The resulting cDNAs were prepared for semi-quantitative real-time PCR using HotStart-IT SYBR Green PCR Kit (Affymetrix) and analyzed in a CFX96 Real-Time PCR Detection System (BioRad) for 40 cycles (95° C for 15 sec, 58° C 30 sec, 72° C for 30 sec) after an initial 2 min incubation at 95° C. Primers were optimized for real-time PCR (amplification efficiency 100 ± 5%). Target gene expression (*NADPH oxidase 1, -2, -4 [Nox1, Nox2, Nox4*]) was normalized against the housekeeping gene *ß2-microglobulin (B2M*), and data were analyzed using the $\Delta\Delta Ct$ method.

Primers: *B2M* forward: 5’ CTGACCGGCCTGTATGCTAT 3’; *B2M* reverse 5’ CAGTCTCAGTGGGGGTGAAT 3’; *Nox1* forward 5’ AATGCCCAGGATCGAGGT 3’; *Nox1* reverse 5’ GATGGAAGCAAAGGGAGTGA 3’; *Nox2* forward 5’ CCCTTTGGTACAGCCAGTGAAGAT 3’; *Nox2* reverse 5’ CAATCCCGGCTCCCACTAACATCA 3’; *Nox4* forward 5’ GGATCACAGAAGGTCCCTAGCAG 3’; *Nox4* reverse 5’ GCGGCTACATGCACACCTGAGAA 3’.

Statistical analyses

The data are presented as mean ± standard error of the mean (s.e.m). The group size for *in vivo* experiments was determined by power analyses using previous muscle specific force data in order to achieve statistical significance with the fewest mice. The mean difference in muscle specific force in mice with breast cancer vs. non-tumor was 42% (275 kN/m^2 vs 390 kN/m^2; s.d. = 64; Fig. 1b). Assuming α error rate = 0.05 and β = 0.20, and a conservative 30% mean difference (275 to 360), the minimum number of animals per group is n = 10. Differences among experimental groups were analyzed by *t*-tests or analysis of variance (ANOVA) with appropriate post hoc and multiple comparison tests. For single time-point measures of any sample size, a two-sided t-test was used[54]. When more than 2 groups were compared simultaneously analysis of variance (ANOVA), followed by Tukey's post hoc tests, were used (e.g. comparison between control, tumor bearing and tumor bearing + S107 groups). In some experiments measurements in a group were repeated over time (for example, forelimb grip). These experiments were analyzed by repeated measures ANOVA followed by Tukey's post hoc tests. *P* values less than 0.05 were considered significant (*P < 0.05; **P < 0.01; ***P < 0.0005; ****P < 0.0001). Statistical analyses were performed with Prism 6.0 software (GraphPad Prism, La Jolla, CA). Samples for semi-quantitative RT-PCR were analyzed with a minimum of 3 biological replicates. Samples for western blot and RT-PCR were analyzed in biological triplicate (minimum). All sample sizes reported in study are minimum values. Assumptions for ANOVA analyses were met (that is, normal distribution) with the exception of data in Figures 1c, 2e, 4f and 5a–b. For these analyses, we used a non-parametric (Kruskal-Wallis) ANOVA and Dunn's multiple comparisons. Variation between groups being compared was not measured due to variability in tumor progression in mice. Exclusion Plan: EDL specific force data was excluded in cases where there was evidence of damage to the muscle fibers. Forelimb grip strength data was excluded when there was evidence of forearm bone lesions since pain likely plays a role in forelimb grip strength and animal compliance. This exclusion plan was pre-established. Female athymic nude mice received from Harlan and female CB.17 SCID mice from Charles River were randomized into groups upon arrival. All statistical tests use biological replicates and indicated by group size (n) in figure legends. Investigators were blinded to the identity of subjects.

Supplementary Material

Refer to Web version on PubMed Central for supplementary material.

ACKNOWLEDGEMENTS

This work was supported by the US National Institutes of Health (U01CA143057 from the NCI Tumor Microenvironment Network and NCI-R01CA69158), the Susan G. Komen Foundation (SAC110013), the Indiana Economic Development Grant, the Jerry and Peggy Throgmartin Endowment of the Indiana University Simon Cancer Center, Indiana University Simon Cancer Center Breast Cancer Program and a generous donation from the Withycombe family (T.A.G.); American Cancer Society and Indiana University Simon Cancer Center (IRG-84-002-28) and the Indiana University Health Strategic Research Initiative in Oncology (D.L.W.); US National Institutes of Health (NHLBI-R01HL061503, NHLBI-R01HL102040, NIAMS-R01AR060037, NIH T32 HL120826, NINDS-R25NS076445), and the Ellison Foundation (A.R.M.); Swedish Heart Lung Foundation and Stockholm County Council (D.C.A.); US National Institutes of Health (NIH-NINDS R25NS076445) (A.H.), and US National Institutes of Health (NIH-NHLBI T35 HL110854-01) (S.C. and P.K.).

REFERENCES

1. Fearon KC, Glass DJ, Guttridge DC. Cancer cachexia: mediators, signaling, and metabolic pathways. Cell Metab. 2012; 16:153–166. [PubMed: 22795476]
2. Gentry BA, Ferreira JA, Phillips CL, Brown M. Hindlimb skeletal muscle function in myostatin-deficient mice. Muscle Nerve. 2011; 43:49–57. [PubMed: 21082689]
3. Mendias CL, Marcin JE, Calerdon DR, Faulkner JA. Contractile properties of EDL and soleus muscles of myostatin-deficient mice. J. Appl. Physiol. 2006; 101:898–905. [PubMed: 16709649]
4. Weilbaecher KN, Guise TA, McCauley LK. Cancer to bone: a fatal attraction. Nat. Rev. Cancer. 2011; 11:411–425. [PubMed: 21593787]
5. Coleman RE, et al. Metastasis and bone loss: advancing treatment and prevention. Cancer Treat. Rev. 2010; 36:615–620. [PubMed: 20478658]
6. Kang Y, et al. Breast cancer bone metastasis mediated by the Smad tumor suppressor pathway. Proc. Natl. Acad. Sci. USA. 2005; 102:13909–13914. [PubMed: 16172383]
7. Korpal M, et al. Imaging transforming growth factor-beta signaling dynamics and therapeutic response in breast cancer bone metastasis. Nat. Med. 2009; 15:960–966. [PubMed: 19597504]
8. Tang Y, et al. TGF-beta1-induced migration of bone mesenchymal stem cells couples bone resorption with formation. Nat. Med. 2009; 15:757–765. [PubMed: 19584867]
9. Zalk R, Lehnart SE, Marks AR. Modulation of the ryanodine receptor and intracellular calcium. Annu. Rev. Biochem. 2007; 76:367–385. [PubMed: 17506640]
10. Andersson DC, et al. Ryanodine receptor oxidation causes intracellular calcium leak and muscle weakness in aging. Cell Metab. 2011; 14:196–207. [PubMed: 21803290]
11. Guise TA, et al. Evidence for a causal role of parathyroid hormone-related protein in the pathogenesis of human breast cancer-mediated osteolysis. J. Clin. Invest. 1996; 98:1544–1549. [PubMed: 8833902]
12. Vera-Ramirez L, et al. Free radicals in breast carcinogenesis, breast cancer progression and cancer stem cells. Biological bases to develop oxidative-based therapies. Crit. Rev. Oncol. Hematol. 2011; 80:347–368. [PubMed: 21288735]
13. Bellinger AM, et al. Hypernitrosylated ryanodine receptor calcium release channels are leaky in dystrophic muscle. Nat. Med. 2009; 15:325–330. [PubMed: 19198614]
14. Lu X, Kang Y. Efficient acquisition of dual metastasis organotropism to bone and lung through stable spontaneous fusion between MDA-MB-231 variants. Proc. Natl. Acad. Sci. USA. 2009; 106:9385–9390. [PubMed: 19458257]
15. Guise TA, Yoneda T, Yates AJ, Mundy GR. The combined effect of tumor-produced parathyroid hormone-related protein and transforming growth factor-alpha enhance hypercalcemia in vivo and bone resorption in vitro. J. Clin. Endocrinol. Metab. 1993; 77:40–45. [PubMed: 8325957]
16. Hjorth-Hansen H, et al. Marked osteoblastopenia and reduced bone formation in a model of multiple myeloma bone disease in severe combined immunodeficiency mice. J. Bone Miner. Res. 1999; 14:256–263. [PubMed: 9933480]
17. Bellinger AM, et al. Remodeling of ryanodine receptor complex causes “leaky” channels: a molecular mechanism for decreased exercise capacity. Proc. Natl. Acad. Sci. USA. 2008; 105:2198–2202. [PubMed: 18268335]
18. Andersson DC, Marks AR. Fixing ryanodine receptor Ca leak - a novel therapeutic strategy for contractile failure in heart and skeletal muscle. Drug Discov. Today Dis. Mech. 2010; 7:e151–e157. [PubMed: 21113427]
19. Dallas SL, Rosser JL, Mundy GR, Bonewald LF. Proteolysis of latent transforming growth factor-beta (TGF-beta)-binding protein-1 by osteoclasts. A cellular mechanism for release of TGF-beta from bone matrix. J. Biol. Chem. 2002; 277:21352–21360. [PubMed: 11929865]
20. Kang Y, et al. A multigenic program mediating breast cancer metastasis to bone. Cancer Cell. 2003; 3:537–549. [PubMed: 12842083]
21. Yin JJ, et al. TGF-beta signaling blockade inhibits PTHrP secretion by breast cancer cells and bone metastases development. J. Clin. Invest. 1999; 103:197–206. [PubMed: 9916131]

22. Shi Y, Massague J. Mechanisms of TGF-beta signaling from cell membrane to the nucleus. Cell. 2003; 113:685–700. [PubMed: 12809600]
23. Dasch JR, Pace DR, Waegell W, Inenaga D, Ellingsworth L. Monoclonal antibodies recognizing transforming growth factor-beta. Bioactivity neutralization and transforming growth factor beta 2 affinity purification. J. Immunol. 1989; 142:1536–1541. [PubMed: 2537357]
24. Biswas S, et al. Anti-transforming growth factor ss antibody treatment rescues bone loss and prevents breast cancer metastasis to bone. PLoS One. 2011; 6:e27090. [PubMed: 22096521]
25. Sun QA, et al. Oxygen-coupled redox regulation of the skeletal muscle ryanodine receptor-Ca2+ release channel by NADPH oxidase 4. Proc. Natl. Acad. Sci. USA. 2011; 108:16098–16103. [PubMed: 21896730]
26. Carmona-Cuenca I, et al. Upregulation of the NADPH oxidase NOX4 by TGF-beta in hepatocytes is required for its pro-apoptotic activity. J. Hepatol. 2008; 49:965–976. [PubMed: 18845355]
27. Hubackova S, Krejcikova K, Bartek J, Hodny Z. IL1- and TGFbeta-Nox4 signaling, oxidative stress and DNA damage response are shared features of replicative, oncogene-induced, and drug-induced paracrine 'bystander senescence'. Aging (Albany NY). 2012; 4:932–951. [PubMed: 23385065]
28. Michaeloudes C, Sukkar MB, Khorasani NM, Bhavsar PK, Chung KF. TGF-beta regulates Nox4, MnSOD and catalase expression, and IL-6 release in airway smooth muscle cells. Am. J. Physiol. Lung Cell Mol. Physiol. 2011; 300:L295–304. [PubMed: 21131394]
29. Yan F, et al. Nox4 and redox signaling mediate TGF-beta-induced endothelial cell apoptosis and phenotypic switch. Cell Death Dis. 2014; 5:e1010. [PubMed: 24457954]
30. Jiang JX, et al. Liver fibrosis and hepatocyte apoptosis are attenuated by GKT137831, a novel NOX4/NOX1 inhibitor in vivo. Free Radic. Biol. Med. 2012; 53:289–296. [PubMed: 22618020]
31. Janssens K, et al. Mutations in the gene encoding the latency-associated peptide of TGF-beta 1 cause Camurati-Engelmann disease. Nat. Genet. 2000; 26:273–275. [PubMed: 11062463]
32. Janssens K, ten Dijke P, Ralston SH, Bergmann C, Van Hul W. Transforming growth factor-beta 1 mutations in Camurati-Engelmann disease lead to increased signaling by altering either activation or secretion of the mutant protein. J. Biol. Chem. 2003; 278:7718–7724. [PubMed: 12493741]
33. Mendias CL, et al. Transforming growth factor-beta induces skeletal muscle atrophy and fibrosis through the induction of atrogin-1 and scleraxis. Muscle Nerve. 2012; 45:55–59. [PubMed: 22190307]
34. Zhou X, et al. Reversal of cancer cachexia and muscle wasting by ActRIIB antagonism leads to prolonged survival. Cell. 2010; 142:531–543. [PubMed: 20723755]
35. McPherron AC, Lawler AM, Lee SJ. Regulation of skeletal muscle mass in mice by a new TGF-beta superfamily member. Nature. 1997; 387:83–90. [PubMed: 9139826]
36. Bogdanovich S, et al. Functional improvement of dystrophic muscle by myostatin blockade. Nature. 2002; 420:418–421. [PubMed: 12459784]
37. Wehrens XH, et al. Protection from cardiac arrhythmia through ryanodine receptor-stabilizing protein calstabin2. Science. 2004; 304:292–296. [PubMed: 15073377]
38. Dunn LK, et al. Hypoxia and TGF-beta drive breast cancer bone metastases through parallel signaling pathways in tumor cells and the bone microenvironment. PLoS One. 2009; 4:e6896. [PubMed: 19727403]
39. Soule HD, Vazguez J, Long A, Albert S, Brennan M. A human cell line from a pleural effusion derived from a breast carcinoma. J. Natl. Cancer Inst. 1973; 51:1409–1416. [PubMed: 4357757]
40. Yin JJ, et al. A causal role for endothelin-1 in the pathogenesis of osteoblastic bone metastases. Proc. Natl. Acad. Sci. USA. 2003; 100:10954–10959. [PubMed: 12941866]
41. Hu Z, et al. Systemic delivery of oncolytic adenoviruses targeting transforming growth factor-beta inhibits established bone metastasis in a prostate cancer mouse model. Hum. Gene Ther. 2012; 23:871–882. [PubMed: 22551458]
42. Johnson RW, et al. Wnt signaling induces gene expression of factors associated with bone destruction in lung and breast cancer. Clin. Exp. Metastasis. 2014; 31:945–959. [PubMed: 25359619]

43. Jackson N, et al. Two new IgA1-kappa plasma cell leukaemia cell lines (JJN-1 & JJN-2) which proliferate in response to B cell stimulatory factor 2. Clin. Exp. Immunol. 1989; 75:93–99. [PubMed: 2495201]
44. Bonetto A, Andersson DC, Waning DL. Assessment of muscle mass and strength in mice. BoneKEy Rep. 2015; 4:732. [PubMed: 26331011]
45. Yamada T, et al. Impaired myofibrillar function in the soleus muscle of mice with collagen-induced arthritis. Arthritis Rheum. 2009; 60:3280–3289. [PubMed: 19877058]
46. Aydin J, et al. Increased mitochondrial Ca2+ and decreased sarcoplasmic reticulum Ca2+ in mitochondrial myopathy. Hum. Mol. Genet. 2009; 18:278–288. [PubMed: 18945718]
47. Lai X, et al. Characterization of the renal cyst fluid proteome in autosomal dominant polycystic kidney disease (ADPKD) patients. Proteomics Clin. Appl. 2008; 2:1140–1152. [PubMed: 20411046]
48. Keller A, Nesvizhskii AI, Kolker E, Aebersold R. Empirical statistical model to estimate the accuracy of peptide identifications made by MS/MS and database search. Anal. Chem. 2002; 74:5383–5392. [PubMed: 12403597]
49. Nesvizhskii AI, Keller A, Kolker E, Aebersold R. A statistical model for identifying proteins by tandem mass spectrometry. Anal. Chem. 2003; 75:4646–4658. [PubMed: 14632076]
50. Lai X, Wang L, Tang H, Witzmann FA. A novel alignment method and multiple filters for exclusion of unqualified peptides to enhance label-free quantification using peptide intensity in LC-MS/MS. J. Proteome Res. 2011; 10:4799–4812. [PubMed: 21888428]
51. Mohammad KS, et al. Pharmacologic inhibition of the TGF-beta type I receptor kinase has anabolic and anti-catabolic effects on bone. PLoS One. 2009; 4:e5275. [PubMed: 19357790]
52. Kimura Y, Kurzydlowski K, Tada M, MacLennan DH. Phospholamban regulates the Ca2+-ATPase through intramembrane interactions. J. Biol. Chem. 1996; 271:21726–21731. [PubMed: 8702967]
53. Cheng H, et al. Amplitude distribution of calcium sparks in confocal images: theory and studies with an automatic detection method. Biophys. J. 1999; 76:606–617. [PubMed: 9929467]
54. de Winter, JCF. Using the student's t-test with extremely small sample sizes.. Practical Assessment, Research & Evaluation 18. 2013. Available online: http://pareonline.net/getvn.asp?v=18&n=10

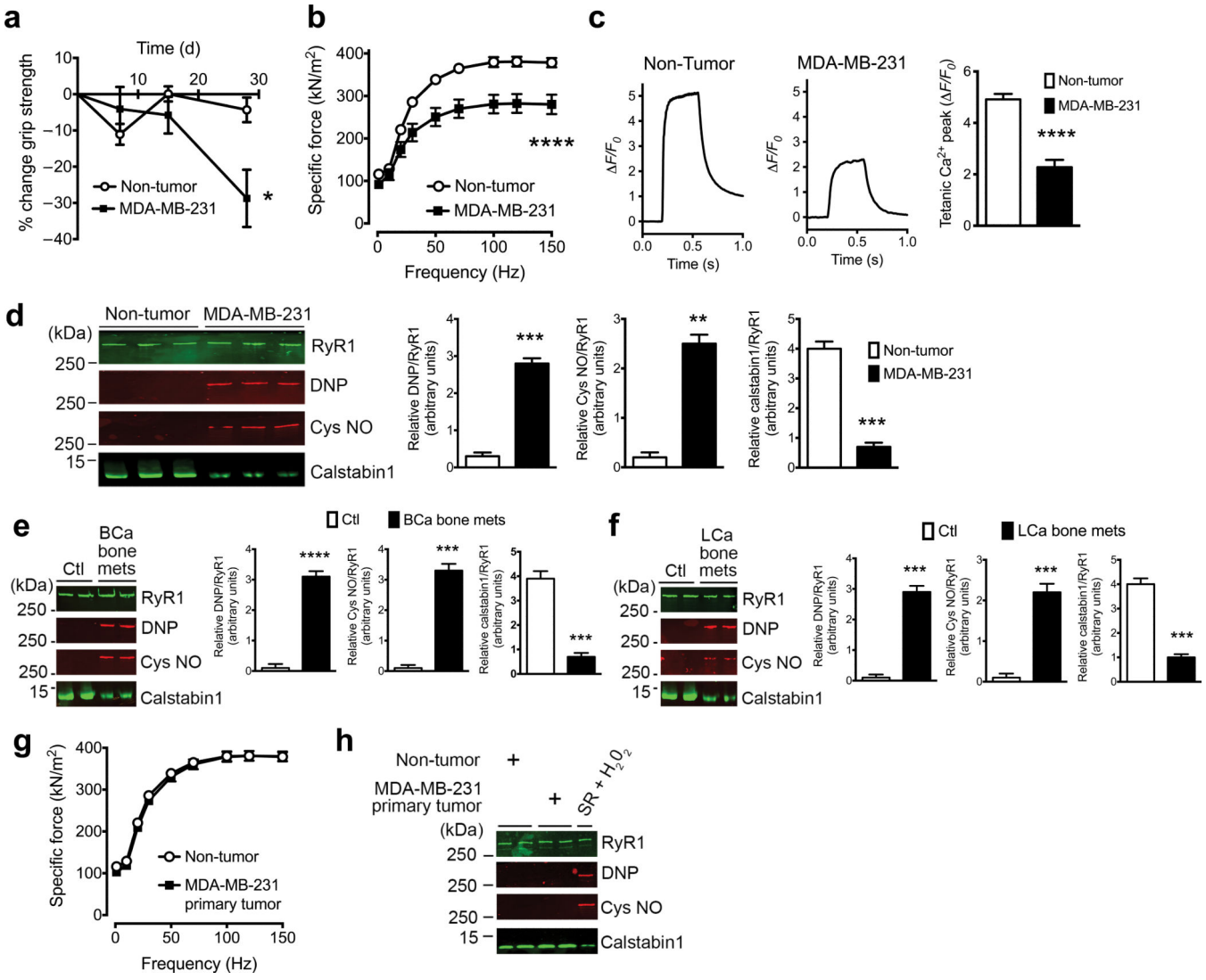

Figure 1.

Skeletal muscle weakness is due to breast cancer bone metastases. (**a**) *In vivo* forelimb grip strength ($n = 10$) and (**b**) *ex vivo* specific force of the extensor digitorum longus (EDL) muscle in mice with MDA-MB-231 breast cancer bone metastases ($n = 10$). (**c**) Tetanic Ca^{2+} peak (Fluo-4) in isolated flexor digitorum brevis (FDB) muscle fibers. Representative single traces (left) and quantitation from $n = 25$ fibers (right). (**d**) Immunoblot of RyR1 oxidation (DNP) and nitrosylation (Cys NO), and RyR1-calstabin1 binding measured by co-immunoprecipitation from EDL muscle and quantitation (right). ($n = 3$). (**e–f**) RyR1 oxidation, nitrosylation and RyR1-calstabin1 binding in muscle samples from humans with (**e**) breast cancer bone metastases (BCa bone mets) or control samples (Ctl) and quantitation (right) ($n = 4$) and (**f**) lung cancer bone metastases (LCa bone mets) and quantitation (right) ($n = 4$). (**g**) *Ex vivo* EDL specific force in mice with primary MDA-MB-231 breast cancer compared to non-tumor control mice ($n = 9$). (**h**) RyR1 oxidation and nitrosylation and RyR1-calstabin1 binding in mice with primary breast cancer and quantitation (right) ($n = 9$). SR + H_2O_2 = sarcoplasmic reticulum preparations treated with hydrogen peroxide. Data are

mean ± s.e.m., (**a**,**b**,**g**) Two-way ANOVA; (**c–f**) t-test; *$P < 0.05$, **$P < 0.01$, ***$P < 0.001$, ****$P < 0.0001$.

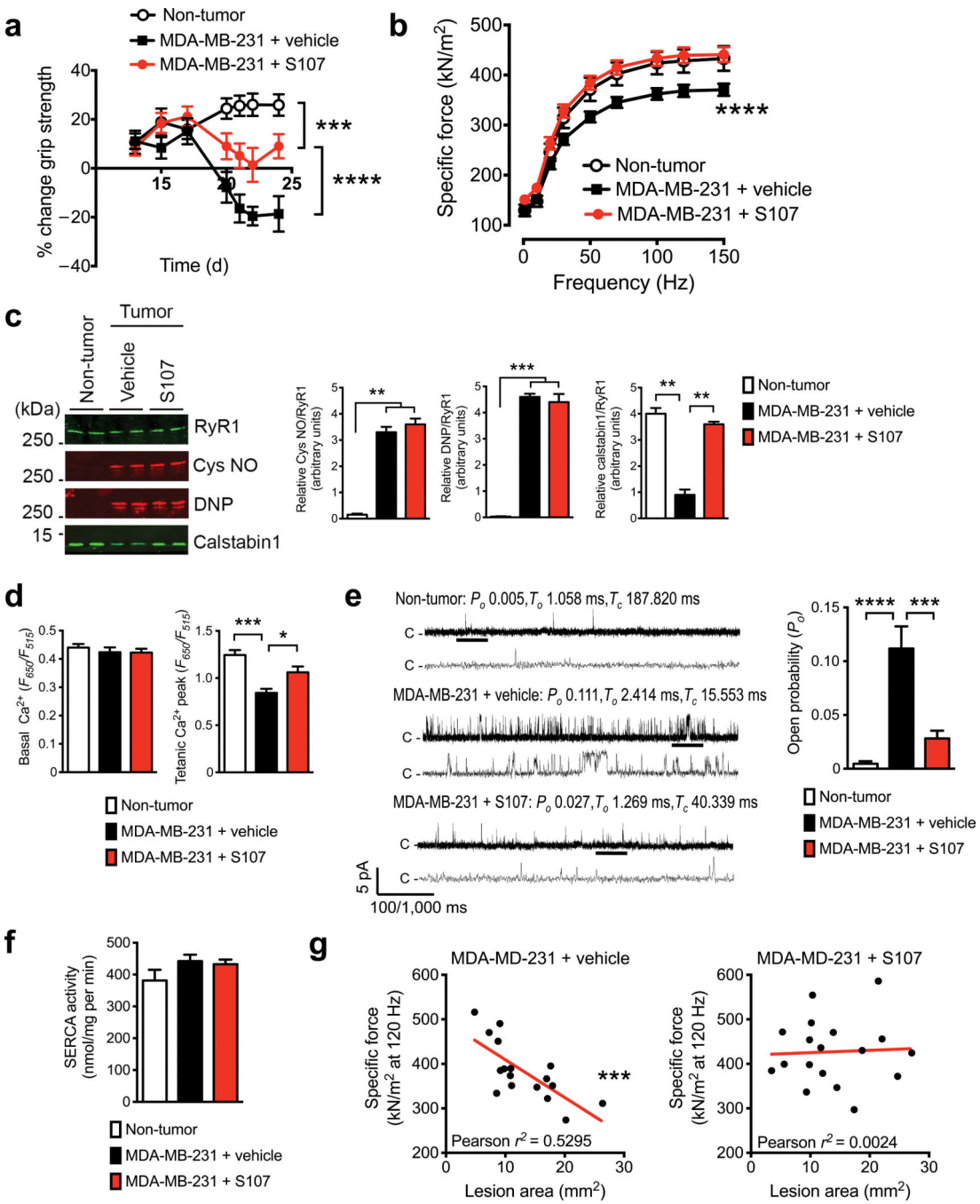

Figure 2.

Rycal S107 improved muscle strength and lowered SR Ca^{2+} leak. (**a**) *In vivo* forelimb grip strength (n = 9) and (**b**) *ex vivo* specific force of the extensor digitorum longus (EDL) muscle in mice with MDA-MB-231 breast cancer bone metastases and receiving S107 treatment (n = 9). (**c**) Immunoblot of RyR1 oxidation (DNP) and nitrosylation (Cys NO), and RyR1-calstabin1 binding measured by co-immunoprecipitation from EDL muscle and quantitation (right) (n = 4). (**d**) Peak tetanic Ca^{2+} amplitude in mice with MDA-MB-231 bone metastases receiving S107 treatment (ratiometric imaging using Fluo-4 and Fura-red)

in flexor digitorum brevis (FDB) muscle fibers (n = 36 fibers). (**e**) RyR1 channel open probability in muscle from mice with MDA-MB-231 bone metastases receiving S107 treatment. Representative single-channel current traces of skeletal RyR1 channels. Channel openings are shown as upward deflections. P_o = open probability, T_o = average open time, T_c = average closed time. The activity of the channel indicated by the thick black bar is shown below on the expanded time scale. Quantification (right) of traces from n = 4 channel recordings. (**f**) SERCA activity from muscle of mice with bone metastases and treated with S107 (n = 4). (**g**) Correlation between maximum specific force (120 Hz) and osteolytic lesion area (measured in all limbs by X-ray imaging) in muscle from mice with MDA-MB-231 bone metastases receiving vehicle or S107. Data are mean ± s.e.m., (**a**,**b**) Two-way ANOVA; (**c–f**) One-way ANOVA with multiple comparisons; (**g**) Pearson's correlation. *P < 0.05, **P < 0.01, ***P < 0.001, ****P < 0.0001.

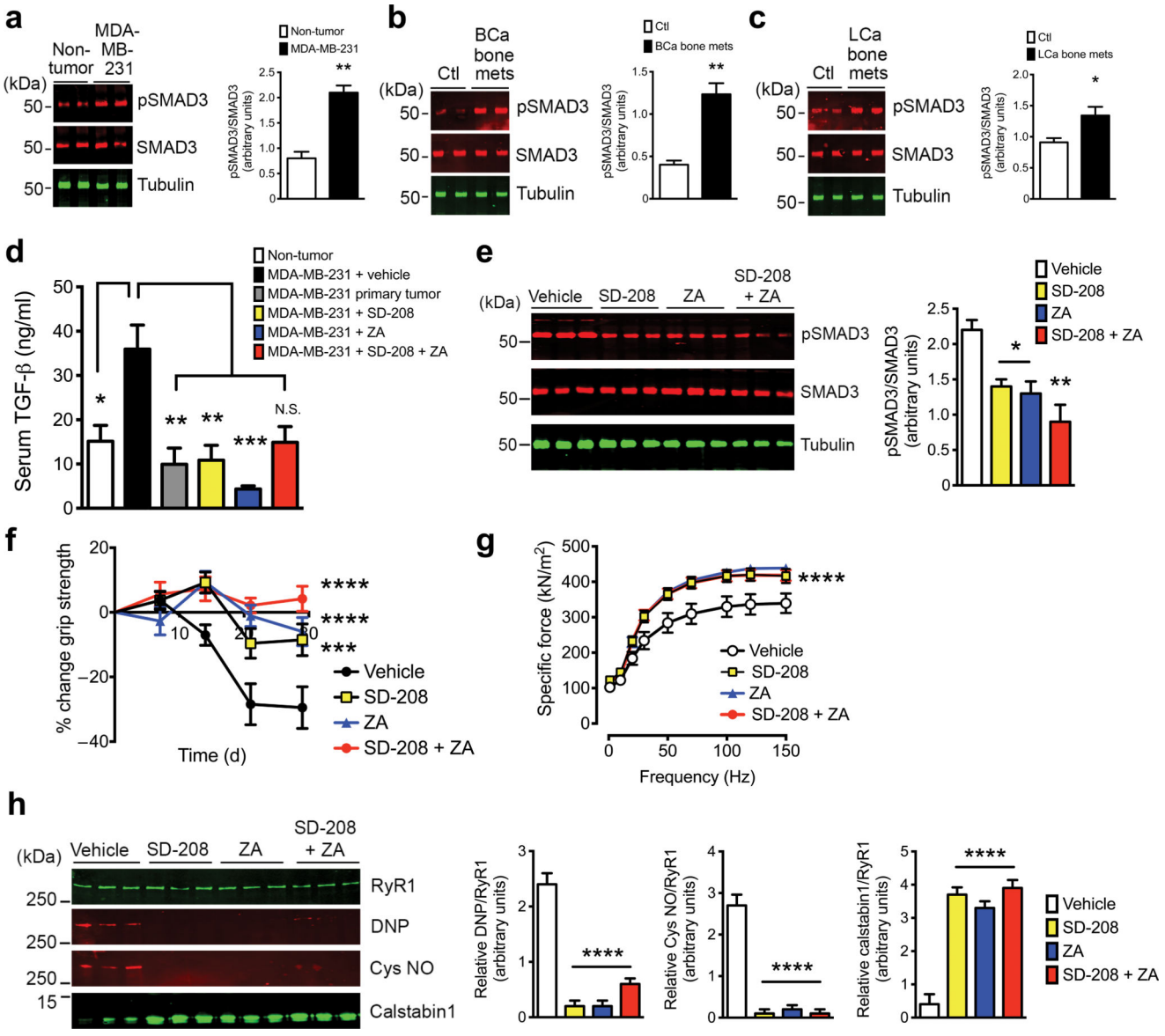

Figure 3.

Blocking TGF-β signaling or inhibiting bone resorption lowered SMAD3 phosphorylation and improved muscle function. SMAD3 phosphorylation in (**a**) muscle from mice with MDA-MB-231 bone metastases and quantitation (right) (*n* = 4), (**b**) muscle samples from humans with breast cancer bone metastases (BCa bone mets) or control samples (Ctl) and quantitation (right) (*n* = 4) and (**c**) lung cancer bone metastases (LCa bone mets) and quantitation (right) (*n* = 4). (**d**) Serum TGF-β concentration in non-tumor mice, mice with MDA-MB-231 bone metastases, MDA-MB-231 primary tumor or mice with MDA-MB-231 bone metastases receiving treatment to block TGF-β signaling (SD-208) or bone resorption (zoledronic acid [ZA]) (*n* = 5). N.S. = not significant. (**e**) SMAD3 phosphorylation in mice with MDA-MB-231 bone metastases receiving either SD-208, ZA or combined therapy (*n* = *3*). (**f**) *In vivo* forelimb grip strength (*n* = 12) and **(g)** *ex vivo* specific force of the extensor digitorum longus (EDL) in mice treated with SD-208, ZA or combined treatment (*n* = 12).

(**h**) Immunoblot of RyR1 oxidation (DNP) and nitrosylation (Cys NO), and RyR1-calstabin1 binding measured by co-immunoprecipitation from EDL muscle and quantitation (right) (*n* = 3). Data are mean ± s.e.m., (**a–c**) t-test; (**d–e**,**h**) One-way ANOVA with multiple comparisons; (**f–g**) Two-way ANOVA. ***P* < 0.01, ****P* < 0.001, *****P* < 0.0001.

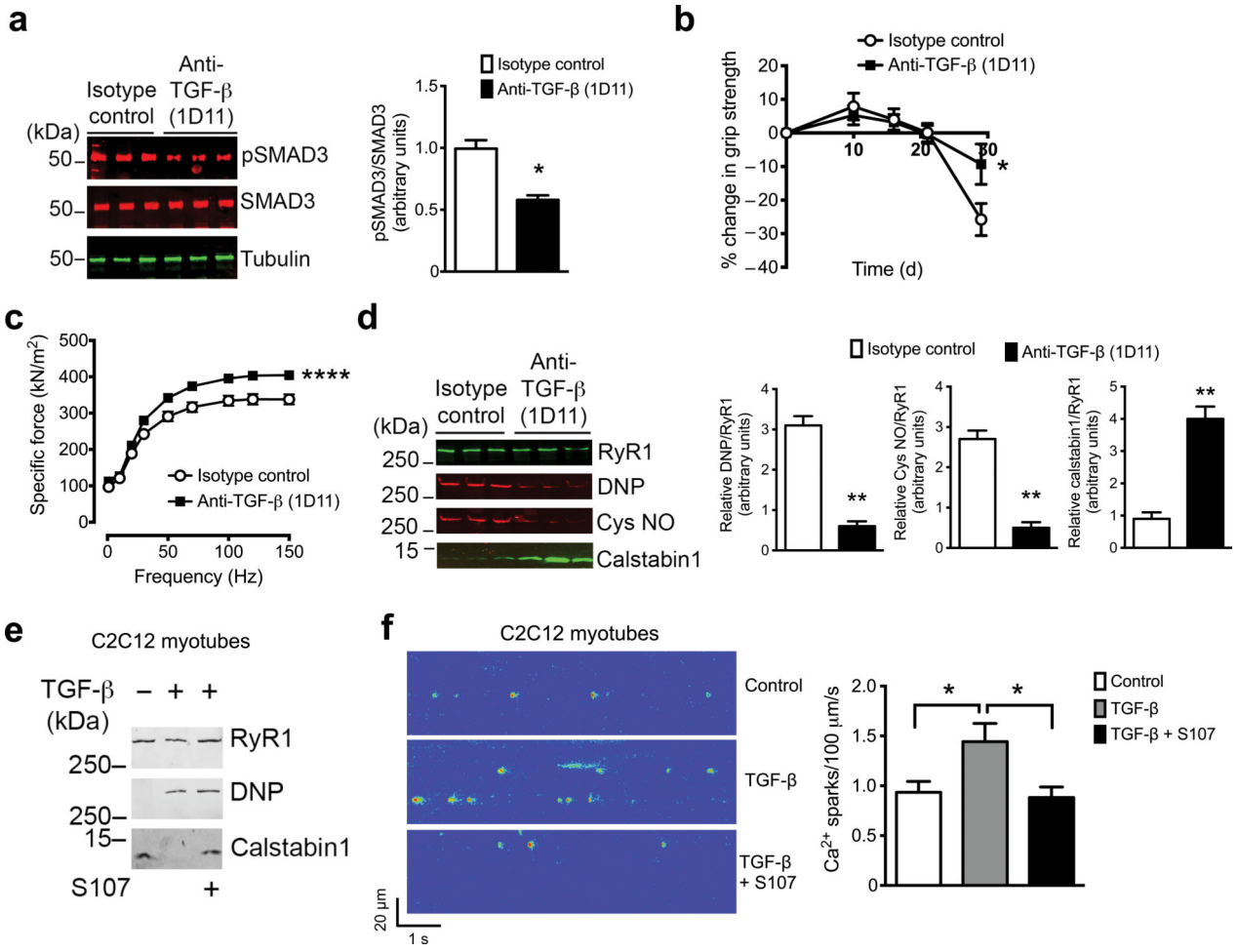

Figure 4.

Blocking TGF-β ligand lowered SMAD3 phosphorylation and improved muscle function. (**a**) SMAD3 phosphorylation in muscle from mice with MDA-MB-231 bone metastases receiving 1D11 and quantitation (right) (*n* = *3*). (**b**) *In vivo* forelimb grip strength (*n* = 11) and (**c**) *ex vivo* specific force of the EDL mice treated with anti-TGF-β neutralizing antibody (clone 1D11) (*n* = 11). (**d**) Immunoblot of RyR1 oxidation (DNP) and nitrosylation (Cys NO), and RyR1-calstabin1 binding measured by co-immunoprecipitation from EDL muscle and quantitation (right) (*n* = 3). (**e**) Immunoblot of RyR1 oxidation and RyR1-calstabin1 binding in C2C12 cells treated with TGF-β or TGF-β + S107. (**f**) Ca^{2+} sparks in C2C12 myotubes treated with TGF-β or TGF-β + S107 (*n* = 52 cells). Data are mean ± s.e.m., (**a**,**d**) t-test; (**b**,**c**) Two-way ANOVA. (**f**) One-way ANOVA with multiple comparisons. **P* < 0.05, ***P* < 0.01, *****P* < 0.0001.

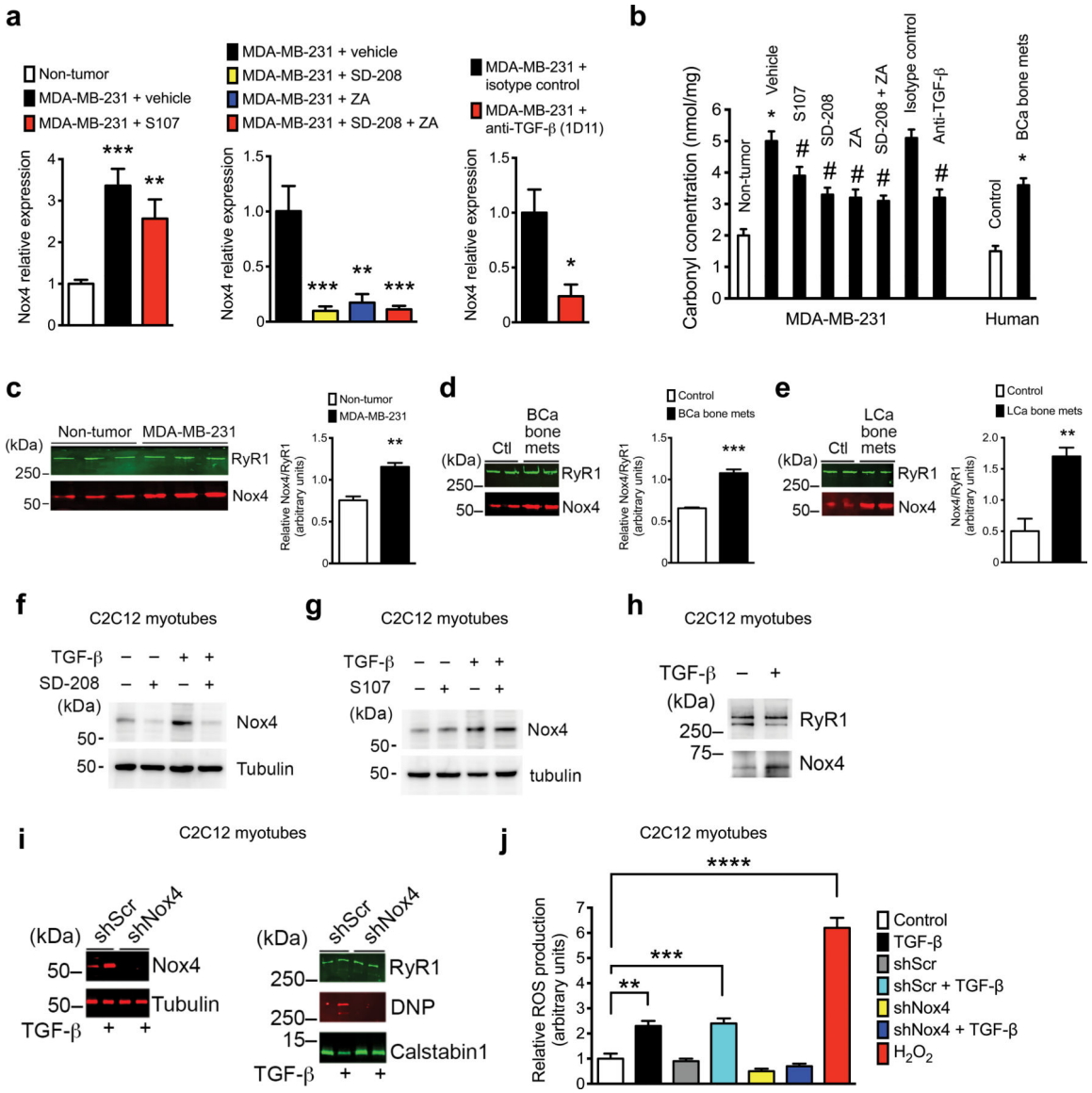

Figure 5.

TGF-β led to higher NADPH oxidase 4 (Nox4) expression and RyR1-Nox4 interaction. (**a**) *Nox4* mRNA expression in tibialis anterior (TA) muscle of mice with MDA-MB-231 breast cancer bone metastases and treated with S107 (left), treated with SD-208 or zoledronic acid (center), or treated with anti-TGF-β antibody (right) (*n* = 3 each group). (**b**) Protein carbonyl concentration in muscle from mice with MDA-MB-231 bone metastases and humans with breast cancer and bone metastases (*n* = 2 for each group). Mean ± s.d.; Two-way ANOVA. **P*<0.05 compared to Non-tumor, #*P*<0.05 compared to vehicle. (**c–e**) Nox4 co-immunoprecipitation with RyR1 in (**c**) muscle from mice with MDA-MB-231 bone metastases (quantitation right) (*n* = 3), (**d**) in muscle samples from humans with breast cancer and bone metastases (BCa bone mets) or control samples (Ctl) (quantitation right) (*n* = *4*) and (**e**) muscle form humans with lung cancer and bone metastases (LCa bone mets) (quantitation right) (*n* = 4). (**f**) Nox4 expression in C2C12 myotubes treated with TGF-β or

TGF-β + SD-208. (**g**) Nox4 expression in C2C12 myotubes treated with TGF-β or TGF-β + S107. (**h**) Nox4 co-immunoprecipitation with RyR1 in C2C12 myotubes treated with TGF-β. (**i**) Immunoblot in C2C12 cells with *Nox4* knock-down (*shNox4* or control *shScr*) (left), RyR1 oxidation (DNP), and RyR1-calstabin1 binding measured by co-immunoprecipitation (right). C2C12 myotubes were either untreated or treated with TGF-β. (**j**) Reactive oxygen species (ROS) generation in C2C12 myotubes. H_2O_2 = hydrogen peroxide ($n = 4$). Data are mean ± s.e.m., (**a–b**,**j**) One-way ANOVA with multiple comparisons; (**c–e**) t-test. *$P < 0.05$, **$P < 0.01$, ***$P < 0.001$, ****$P < 0.0001$.

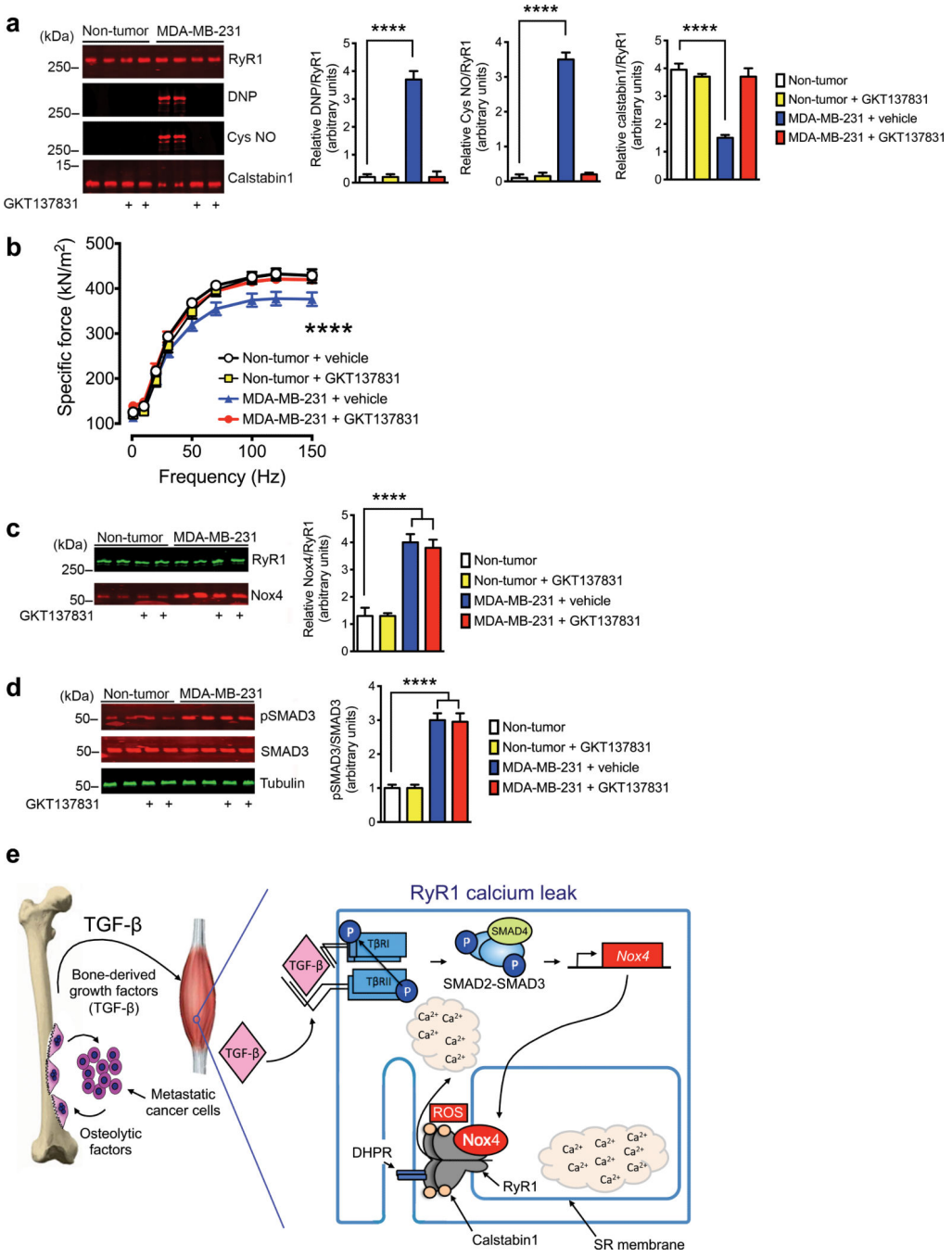

Figure 6.

NADPH oxidase 4 (Nox4) inhibition prevents RyR1 oxidation and improves muscle strength. (**a**) Immunoblot of RyR1 oxidation (DNP) and nitrosylation (Cys NO), and RyR1-calstabin1 binding measured by co-immunoprecipitation from EDL muscle and quantitation (right). (n = 4) from mice with MDA-MB-231 bone metastases and treated with Nox4 inhibitor, GKT137831. (**b**) *Ex vivo* EDL specific force in mice with MDA-MB-231 breast cancer and treated with GKT137831 (n = 8). (**c**) Nox4 co-immunoprecipitation with RyR1 in muscle from mice with MDA-MB-231 bone and treated with GKT137831 (quantitation

right) (n = 4). (**d**) SMAD3 phosphorylation in muscle from mice with MDA-MB-231 bone metastases and treated with GKT137831 (quantitation right) (n = 4). (**e**) Model of the role of TGF-β-induced oxidation and intracellular Ca^{2+} leak in breast cancer-associated muscle weakness. TGF-β liberated from the bone matrix during osteolytic bone destruction drives the expression of *Nox4* in muscle via SMAD2-SMAD3 signaling. Nox4 produces reactive oxygen species (ROS). Oxidation of RyR1 leads to loss of Calstabin1 binding and Ca^{2+} leak from the sarcoplasmic reticulum thus depleting intracellular Ca^{2+} stores causing decreased muscle specific force. Inhibiting TGF-β release from the bone matrix, TGF-β signaling, Nox4 activity, and RyR1-mediated SR Ca^{2+} leak all improved muscle strength. DHPR = dihydropyridine receptor. Data are mean ± s.e.m., (**a**,**c–d**) One-way ANOVA with multiple comparisons; (**b**) Two-way ANOVA. ****$P < 0.0001$.